



Acetylation-dependent regulation of PD-L1 nuclear translocation dictates the efficacy of anti-PD-1 immunotherapy

Yang Gao^{1,2,14}, Naoe Taira Nihira^{1,3,4,14}, Xia Bu^{1,5,14}, Chen Chu^{1,6,7}, Jinfang Zhang¹, Aleksandra Kolodziejczyk^{1,6,7}, Yizeng Fan^{1,2}, Ngai Ting Chan⁸, Leina Ma¹, Jing Liu¹, Dong Wang¹, Xiaoming Dai¹, Huadong Liu⁹, Masaya Ono¹⁰, Akira Nakanishi^{1,3}, Hiroyuki Inuzuka¹, Brian J. North¹, Yu-Han Huang^{11,12}, Samanta Sharma^{6,7}, Yan Geng^{6,7}, Wei Xu^{1,8}, X. Shirley Liu^{1,13}, Lei Li², Yoshio Miki^{1,3,✉}, Piotr Sicinski^{1,6,7,✉}, Gordon J. Freeman^{1,5,✉} and Wenyi Wei^{1,✉}

Immunotherapies that target programmed cell death protein 1 (PD-1) and its ligand PD-L1 as well as cytotoxic T-lymphocyte-associated protein 4 (CTLA4) have shown impressive clinical outcomes for multiple tumours. However, only a subset of patients achieves durable responses, suggesting that the mechanisms of the immune checkpoint pathways are not completely understood. Here, we report that PD-L1 translocates from the plasma membrane into the nucleus through interactions with components of the endocytosis and nucleocytoplasmic transport pathways, regulated by p300-mediated acetylation and HDAC2-dependent deacetylation of PD-L1. Moreover, PD-L1 deficiency leads to compromised expression of multiple immune-response-related genes. Genetically or pharmacologically modulating PD-L1 acetylation blocks its nuclear translocation, reprograms the expression of immune-response-related genes and, as a consequence, enhances the anti-tumour response to PD-1 blockade. Thus, our results reveal an acetylation-dependent regulation of PD-L1 nuclear localization that governs immune-response gene expression, and thereby advocate targeting PD-L1 translocation to enhance the efficacy of PD-1/PD-L1 blockade.

Invasion of immune surveillance is one of the most essential features of tumorigenesis¹. To evade the immune response, activation of two crucial negative regulatory checkpoint pathways, CTLA4 and PD-L1–PD-1, is frequently observed in the tumour microenvironment². Indeed, antibodies against these molecules have exhibited improved clinical outcomes in a variety of human cancers³. However, the response rate is relatively low (15–25%) for several cancer types, and only a subset of patients achieves durable responses⁴. Notably, almost one third of primary responders will relapse over time⁵, suggesting that the mechanisms of the immune checkpoint pathways are not completely understood. Membrane-anchored PD-L1 has been well studied for its engagement with PD-1 on T cells to evade anti-tumour immunity². Expression of PD-L1 is tightly controlled at the transcriptional and post-translational levels; however, aberrant expression of PD-L1 is observed in human cancers^{6–8}. Importantly, it has been suggested that high expression of PD-L1 in tumours is one of the biomarkers for improved sensitivity to PD-1/PD-L1 blockade^{9,10}. However, the

underlying mechanisms of how increased expression of PD-L1 sensitizes the efficiency of PD-1 blockade remain unclear.

Lysine acetylation of non-histone proteins can compete with ubiquitination to affect protein stability or subcellular localization^{11,12}. Notably, acetylation of epidermal growth factor receptor (EGFR), which is mainly expressed on the plasma membrane, by cyclic AMP response element-binding protein (CBP) regulates its clathrin-mediated endocytosis and nuclear localization^{13–15}. PD-L1 is also a plasma membrane protein and undergoes ubiquitination by several ubiquitin E3 ligases^{6,7,16,17}, and acetylation of PD-L1 has been previously suggested¹⁸; however, the regulatory mechanisms and functional effects of the acetylation remain largely unknown.

Here we report that PD-L1 is acetylated at Lys 263 in the cytoplasmic domain by p300 acetyltransferase, and deacetylation of PD-L1 by HDAC2 triggers nuclear translocation by interaction with multiple proteins that are involved in endocytosis and nuclear import. Moreover, nuclear PD-L1 binds to DNA and regulates the expression of multiple immune-response-related genes to modulate

¹Department of Pathology, Beth Israel Deaconess Medical Center, Harvard Medical School, Boston, MA, USA. ²Department of Urology, The First Affiliated Hospital of Xi'an Jiaotong University, Xi'an, China. ³Department of Molecular Genetics, Medical Research Institute, Tokyo Medical and Dental University, Tokyo, Japan. ⁴Division of Pediatric Dentistry, Department of Oral Health and Development Sciences, Tohoku University Graduate School of Dentistry, Sendai, Japan. ⁵Department of Medical Oncology, Dana-Farber Cancer Institute, Harvard Medical School, Boston, MA, USA. ⁶Department of Cancer Biology, Dana-Farber Cancer Institute, Boston, MA, USA. ⁷Department of Genetics, Blavatnik Institute, Harvard Medical School, Boston, MA, USA.

⁸McArdle Laboratory for Cancer Research, University of Wisconsin-Madison, Madison, WI, USA. ⁹Center for Mitochondrial Biology and Medicine, The Key Laboratory of Biomedical Information Engineering of Ministry of Education, School of Life Science and Technology and Frontier Institute of Science and Technology, Xi'an Jiaotong University, Xi'an, China. ¹⁰Department of Clinical Proteomics, National Cancer Center Research Institute, Tokyo, Japan.

¹¹Department of Biomedical Informatics, Harvard Medical School, Boston, MA, USA. ¹²Division of Genetics and Genomics, Boston Children's Hospital, Boston, MA, USA. ¹³Department of Biostatistics and Computational Biology, Dana-Farber Cancer Institute, Boston, MA, USA. ¹⁴These authors contributed equally: Yang Gao, Naoe Taira Nihira, Xia Bu. ✉e-mail: miki.mgen@mri.tmd.ac.jp; peter_sicinski@dfci.harvard.edu; gordon_freeman@dfci.harvard.edu; wwei2@bidmc.harvard.edu

the anti-tumour immune response. Thus, our findings reveal that PD-L1 nuclear localization is regulated in a acetylation-dependent manner, and suggest a strategy for improving the efficacy of PD-1/PD-L1 blockade by targeting PD-L1 translocation.

Results

PD-L1 is acetylated at Lys 263 within its cytoplasmic domain by p300. We observed that acetylation of endogenous PD-L1 was detected by a pan-acetyl lysine antibody in multiple cell lines (Fig. 1a and Extended Data Fig. 1a,b). We next found that ectopic expression of p300 and CBP—but not other acetyltransferases, including GCN5, PCAF or Tip60—promoted the acetylation of PD-L1 (Fig. 1b). However, endogenous acetylation of PD-L1 was reduced by treatment with a selective p300/CBP inhibitor A485 (ref. ¹⁹) or knockdown of *EP300* (which encodes p300), but not *CREBBP* (which encodes CBP; Fig. 1c–e). Furthermore, p300 directly acetylates recombinant PD-L1 in vitro (Fig. 1f). These results demonstrate that p300 might represent a physiological acetyltransferase for PD-L1.

Furthermore, we found that deletion of the cytoplasmic tail (C-tail) of PD-L1 abolished p300-mediated acetylation, suggesting that the acetylation site(s) resides within the C-tail (Fig. 1g,h and Extended Data Fig. 1c,d). To identify the acetylation site(s) on PD-L1, we substituted each of five lysine (K) residues within C-tail into arginine (R) and found that only the K263R mutant failed to be acetylated by p300 (Fig. 1i and Extended Data Fig. 1e). Consistent with this result, an antibody raised against acetyl-K263 PD-L1 specifically recognized the acetylated wild type (WT) PD-L1, but not the acetylation-deficient K263R mutant (Extended Data Fig. 1f–h). Using a synthetic peptide of PD-L1 amino acids 261–270, we confirmed the acetylation of Lys 263 by p300 using mass spectrometry (MS) analysis (Extended Data Fig. 1i). Together, these results indicate that Lys 263 might be the major acetylation site on PD-L1.

HDAC2 specifically interacts with and deacetylates PD-L1. Acetyltransferases and their counteracting deacetylases are important for controlling various cellular processes²⁰. To identify the potential physiological deacetylase(s) for PD-L1, we treated cells with the deacetylase inhibitors and found that trichostatin A (TSA), an inhibitor of histone deacetylases (HDACs)—but not of nicotinamide (NIC), which is a class-III sirtuin deacetylase (SIRT) inhibitor—increased acetylation of PD-L1 (Fig. 2a). Consistent with this notion, we found that only HDAC2, but not other HDACs or SIRTs, exhibited a physical interaction with PD-L1 (Fig. 2b and Extended Data Fig. 2a). Furthermore, ectopic expression of HDAC2, but not other HDACs, decreased p300-mediated acetylation of PD-L1 (Fig. 2c,d). By contrast, depletion of endogenous HDAC2 using short interfering RNA (siRNA), short hairpin RNA (shRNA) or CRISPR–Cas9 increased acetylation of PD-L1 (Fig. 2e–g). In line with this, the selective HDAC2 inhibitor santacruzamate A (SCA)²¹ and the HDAC1/2 inhibitor ACY957, but not the HDAC6 inhibitor ACY1215, increased acetylation of endogenous PD-L1

(Fig. 2h), supporting the notion that HDAC2 is a bona fide deacetylase for PD-L1. Importantly, we found that the HDAC2 inhibitor could increase PD-L1 acetylation levels in the WT cells, but not in *HDAC2*-knockout (KO) cells, suggesting that the activity of the HDAC2 inhibitor is specific (Fig. 2i).

Lys 263 acetylation affects the translocation of PD-L1 into the nucleus. Protein acetylation of lysine residues could antagonize ubiquitination of lysine residues to affect protein stability, dimerization or subcellular localization^{11,12}. However, *HDAC2* deficiency minimally affected the PD-L1 poly-ubiquitination (Extended Data Fig. 2b). Moreover, there were no detectable changes in protein half-lives or dimerization among WT and acetylation-deficient PD-L1^{K263R} and acetylation-mimetic PD-L1^{K263Q} mutants (Extended Data Fig. 2c–e). Interestingly, cellular fractionation assays using two commercial kits and immunofluorescence analysis of endogenous PD-L1 revealed that, in addition to the expected membrane-localized species of PD-L1, a notable portion of PD-L1 was also detected in the nucleus and cytoskeleton in human and mouse cancer cell lines using different commercial PD-L1 antibodies (Fig. 3a,b and Extended Data Fig. 3a–f). We also observed this finding in normal non-transformed cells, such as macrophages and mouse embryonic fibroblasts (MEFs; Extended Data Fig. 3g,h).

Notably, we found that deletion of the C-tail largely abolished nuclear localization of PD-L1 (Fig. 3c,d and Extended Data Fig. 3i,j). Moreover, the acetylation-mimetic PD-L1^{K263Q} mutant was compromised in its nuclear localization in both human and mouse cells (Fig. 3e,f and Extended Data Fig. 3k), suggesting that Lys 263 acetylation might block PD-L1 nuclear localization. Furthermore, nuclear PD-L1 was relatively less acetylated when comparing the acetylation status in each fraction (Extended Data Fig. 3l). Moreover, genetic depletion or pharmacologic inhibition of HDAC2 reduced the nuclear portion of PD-L1 (Fig. 3g–i and Extended Data Fig. 3m,n), probably due to an increase in PD-L1 acetylation at Lys 263 (Figs. 2g and 3h). Taken together, these findings suggest that acetylation of Lys 263 on PD-L1 has a critical role in the nuclear-translocation process. Interestingly, lung metastases derived from B16F10 cells displayed relatively stronger nuclear PD-L1 expression compared with B16F10-derived subcutaneous primary tumours in which PD-L1 is predominantly expressed on the membrane (Fig. 3j,k), suggesting that nuclear PD-L1 accumulation might facilitate tumour cells to evade the immune surveillance during the metastatic process.

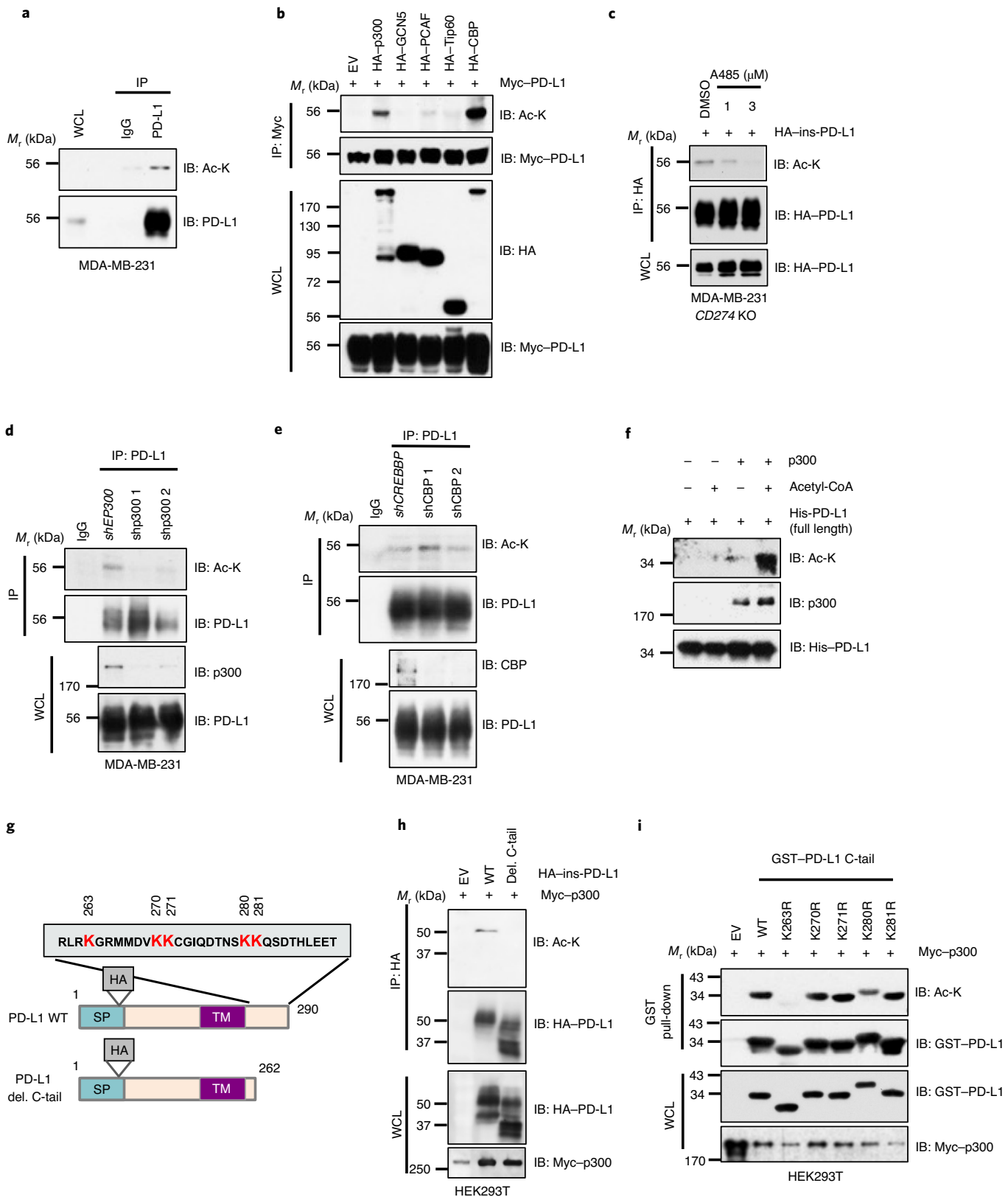
Clathrin-dependent endocytosis of PD-L1 requires interaction with HIP1R. We next examined the molecular mechanisms of how PD-L1 translocates from the plasma membrane to the nucleus. As the C-tail of PD-L1 lacks a canonical nuclear localization sequence, we hypothesized that adaptor protein(s) might be required for PD-L1 nuclear translocation. To this end, we identified around 400 proteins as PD-L1-binding molecules using MS, and Gene Ontology (GO) analysis revealed that these molecules

Fig. 1 | PD-L1 is acetylated at Lys 263 by p300. **a**, Immunoblot (IB) analysis of whole-cell lysates (WCL) and anti-PD-L1 immunoprecipitates (IPs) derived from MDA-MB-231 cells. IgG was used as a negative control. *M_r*, relative molecular mass. Ac-K, acetylated lysine. **b**, IB analysis of WCL and anti-Myc IPs derived from HEK293T cells transfected with Myc-PD-L1 and HA-tagged p300, GCN5, PCAF, Tip60 or CBP. **c**, IB analysis of WCL and anti-HA IPs derived from MDA-MB-231 CD274-KO cells reintroduced with HA-ins-PD-L1 (HA-tag was inserted into PD-L1 protein after the signal peptide sequence. ins, inserted) and treated with dimethylsulfoxide (DMSO) or the indicated concentration of A485 for 4 h. **d**, IB analysis of WCL and anti-PD-L1 IPs derived from MDA-MB-231 cells transduced with shRNAs against *EP300* or GFP as negative control. **e**, IB analysis of WCL and anti-PD-L1 IPs derived from MDA-MB-231 cells transduced with shRNAs against *CREBBP* or GFP as a negative control. **f**, In vitro acetylation assay using purified His-PD-L1 recombinant protein incubated with p300 in the presence or absence of acetyl-CoA. **g**, Schematic of the PD-L1 protein domains and amino acid residues in the cytoplasmic domain (C-tail). SP, signal peptide; TM, transmembrane domain. **h**, IB analysis of WCL and anti-HA IPs derived from HEK293T cells transfected with Myc-p300 and HA-PD-L1 (wild type (WT)) or the deletion mutant of the C-tail (amino acids 263–290). **i**, IB analysis of WCL and glutathione S-transferase (GST) pull-down products derived from HEK293T cells transfected with Myc-p300 and GST-tagged C-tail PD-L1 or K (lysine) to R (arginine) mutants. For the western blots in **a–f**, **h** and **i**, *n*=2 independent experiments were performed with similar results. Source data are available online.

were involved in endocytosis, nuclear transport and export pathways (Fig. 4a,b, Extended Data Fig. 4a and Supplementary Tables 1–3). We further investigated the molecular mechanisms that underlie PD-L1 nuclear trafficking, and found that Pitstop²², which is an inhibitor of clathrin-dependent endocytosis, but not Fillip III (ref. ²³), which is an inhibitor of Caveolae-mediated endocytosis²⁴,

blocked the nuclear localization of PD-L1 (Fig. 4c), suggesting that clathrin-dependent endocytosis might represent an initial step for the nuclear translocation of PD-L1.

Clathrin-dependent endocytosis requires adaptor proteins that recognize endocytic sorting sequences in the cytosolic domains of transmembrane proteins²⁵. However, PD-L1 does not harbour the



typical endocytic signal sequences, indicating the involvement of anchoring proteins that link PD-L1 to clathrin-mediated endocytosis. A recent study showed that huntingtin-interacting-protein-1-related (HIP1R) protein, which was also identified in our MS analysis (Supplementary Table 3), binds to PD-L1 to promote its lysosomal degradation²⁶. We showed that PD-L1 specifically interacted with HIP1R through its C-tail (Fig. 4d,e). Notably, the acetylation-mimetic K263Q mutant was compromised in its interaction with HIP1R (Fig. 4f), indicating that Lys 263 acetylation might block the binding to HIP1R. Consistent with this result, HDAC2 inhibitor treatment disrupted PD-L1 interaction with HIP1R (Extended Data Fig. 4b). Notably, *HIP1R*-KO cells exhibited a substantial decrease in nuclear and cytoskeletal localization of PD-L1 compared with WT cells (Fig. 4g). In the process of protein endocytosis, clathrin selectively binds to cargo adaptors, including the adaptor protein (AP) complex²⁷. Our results further showed that adaptin-β2 (AP2B1) interacted with PD-L1 and recognized HIP1R through a dileucine motif D/E-X-X-X-L/I²⁸ (amino acids 966–979; Fig. 4h–j). Given that PD-L1 is an extensively glycosylated membrane protein¹⁶, we next examined whether glycosylation affects PD-L1 acetylation and nuclear translocation. However, we did not observe notable differences in acetylation levels or nuclear localization between WT and the glycosylation-deficient 4NQ-mutant (N35Q, N192Q, N200Q and N219Q) PD-L1 (Extended Data Fig. 4c,d), indicating that PD-L1 endocytosis is largely independent of its glycosylation status. Thus, these results suggest a model in which HIP1R functions as a bridging protein through the adaptor protein AP2B1 to tether unacetylated PD-L1 to clathrin for endocytosis (Extended Data Fig. 4e).

Interaction with vimentin and importin-α1 facilitates PD-L1 nuclear translocation. Previous reports demonstrated that the cytoskeleton has a critical role in the nucleocytoplasmic shuttling of proteins such as RelA/p65, EGFR and yes-associated protein (YAP)^{29–31}. As our MS analyses showed that PD-L1 interacted with several cytoskeleton proteins, including vimentin (VIM) and Keratins (KRTs; Supplementary Table 3), we further speculated that binding to the cytoskeleton might be important for PD-L1 nucleocytoplasmic translocation. Interestingly, a previous study reported that nuclear PD-L1 was enriched in circulating tumour cells when using vimentin as a sorting marker³². Given that vimentin has a critical role in mediating epithelial-to-mesenchymal transition and metastasis, metastatic cells with high vimentin expression might accumulate nuclear PD-L1 to confer evasion of immune surveillance during metastasis. Indeed, vimentin^{high} cell lines displayed higher PD-L1 expression in cytoskeletal and nuclear soluble fractions compared with vimentin^{low} cell lines (Fig. 5a–c and Extended Data Fig. 4f,g). Mechanistically, PD-L1 interacts with vimentin through the C-tail of PD-L1 (Fig. 5d,e). However, the interaction between PD-L1 and vimentin was not attenuated by the PD-L1^{K263Q} mutation, thereby refuting the possibility that this process is regulated in a PD-L1-acetylation-dependent manner (Fig. 5f). Interestingly, depletion of VIM attenuated PD-L1 expression in cytoskeletal

and nuclear soluble fractions (Fig. 5g and Extended Data Fig. 4h). In support of this notion, induction of vimentin by TGFβ1 treatment³³ enhanced PD-L1 nuclear translocation (Extended Data Fig. 4i,j). Together, these findings demonstrate that nucleocytoplasmic translocation of PD-L1 might occur in a cytoskeleton-dependent manner.

Importin-α family proteins regulate protein nuclear translocation³⁴, and our MS analyses identified various importin components as PD-L1-interacting proteins (Supplementary Table 3). We therefore next focused on the mechanism of nuclear translocation by the importin complex. Treatment of ivermectin³⁵, which is an inhibitor of importin-α/β-dependent nuclear import, reduced the abundance of nuclear PD-L1 (Extended Data Fig. 4k). We also observed that PD-L1 specifically interacted with importin-α1 (IPOA1/KPNA2), but not with importin-α5 and -α7, through the C-tail of PD-L1 (Fig. 5h,i). Importantly, the PD-L1^{K263Q} mutant failed to interact with importin-α1 (Fig. 5j), suggesting that Lys 263 deacetylation is probably critical for the interaction. Thus, we propose a model in which deacetylation of PD-L1 by HDAC2 on the plasma membrane enables PD-L1 to interact with HIP1R and cargo proteins for endocytosis and with vimentin to traffic through the cytoskeleton, and finally translocate into the nucleus through importin-α1 (Extended Data Fig. 4l).

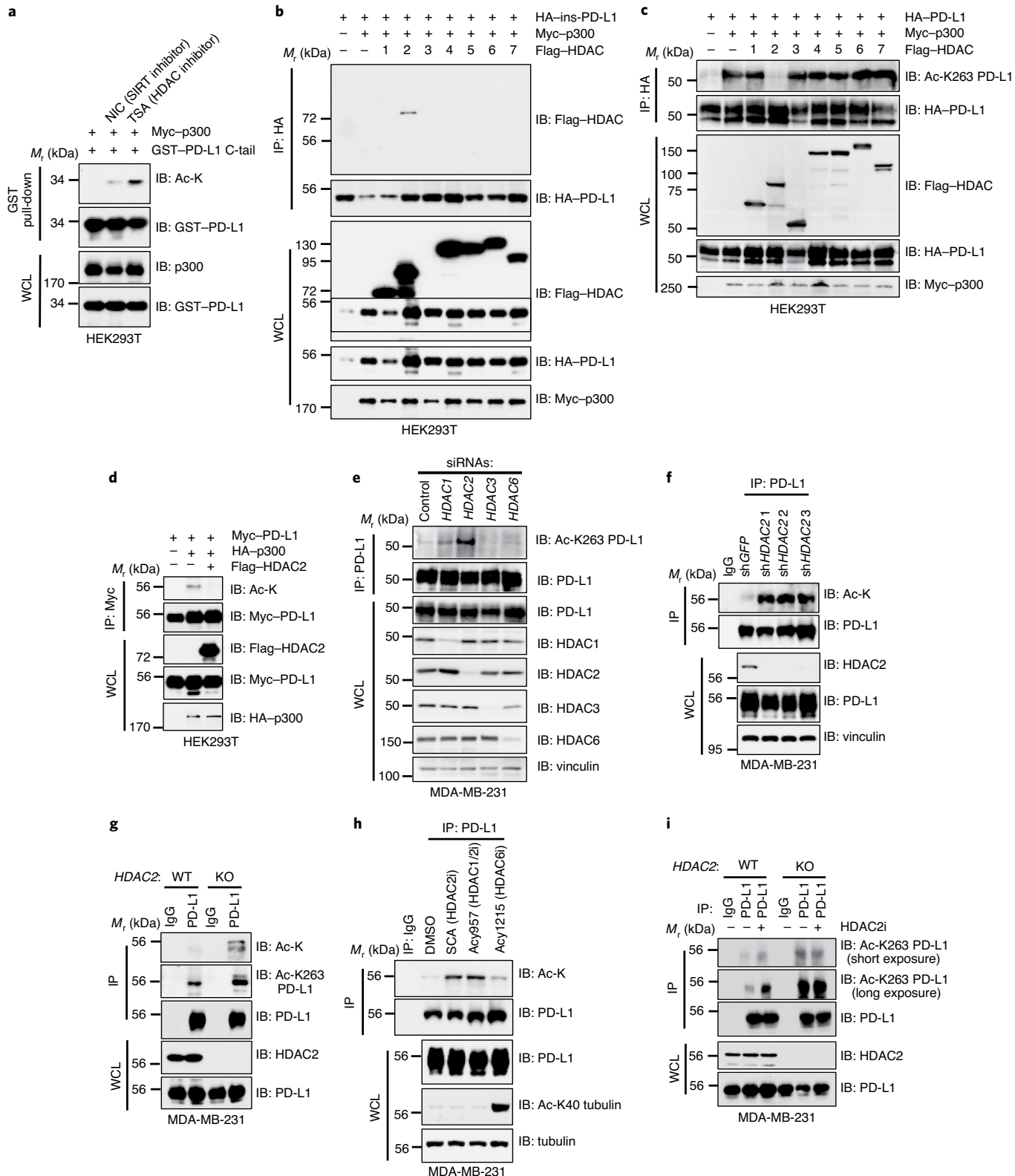
Nuclear PD-L1 regulates gene expression. Previous studies showed that several membrane proteins, including EGFR, insulin receptor and amphiregulin, translocate into the nucleus to regulate gene transcription^{14,36,37}. Notably, consistent with a recent report that PD-L1 interacts with negatively charged RNA³⁸, we found that PD-L1 can directly bind to DNA in vitro and in cells (Extended Data Fig. 5a,b). Both C-tail deletion and treatment with HDAC inhibitor decreased PD-L1 binding to DNA (Extended Data Fig. 5c,d), suggesting that PD-L1 interacts with DNA through the positively charged Lys residues in the C-tail, which undergoes acetylation-mediated inhibition. These results further suggest that PD-L1 might regulate gene transcription through binding to DNA.

To further examine the physiological function of PD-L1 on DNA, we performed RNA-seq analysis to compare the gene expression profiles between *CD274* (which encodes PD-L1) WT and KO cells (Extended Data Fig. 5e). Interestingly, we found that *CD274* deficiency in cancer cells downregulated a panel of immune-response-related genes that are involved in pathways of type-I interferon (IFN) signalling, IFNγ-mediated signalling, NF-κB signalling and antigen processing and presentation by MHC I (Fig. 6a–c, Extended Data Fig. 5f–j, and Supplementary Tables 4 and 5). Indeed, we confirmed that PD-L1 depletion reduced the expression of NF-κB-signalling-related genes and MHC class-I genes using quantitative PCR with reverse transcription (RT-qPCR; Fig. 6d). Furthermore, the results from RNA-seq analysis and RT-qPCR analysis revealed that reintroducing PD-L1 WT, but not the acetylation-mimetic PD-L1^{K262Q} (in mouse) or PD-L1^{K263Q} (in human) mutant, could partially rescue the expression of downregulated IFNs and NF-κB signalling genes in *CD274*-KO cells

Fig. 2 | PD-L1 is deacetylated predominantly by HDAC2. **a**, IB analysis of WCL and GST-pull-down products derived from HEK293T cells transfected with Myc-p300, GST-PD-L1 C-tail in the presence or absence of the SIRT inhibitor (5 mM NIA) or the HDAC inhibitor (1 μM TSA) overnight. **b**, IB analysis of WCL and anti-HA IPs derived from HEK293T cells transfected with Myc-p300, HA-ins-PD-L1 and/or the indicated Flag-tagged deacetylases. **c**, IB analysis of WCL and anti-HA IPs derived from HEK293T cells transfected with the indicated constructs to examine PD-L1 acetylation levels. **d**, IB analysis of WCL and anti-Myc IPs derived from HEK293T cells transfected with HA-p300, Myc-PD-L1 and/or Flag-HDAC2. **e**, IB analysis of WCL and anti-PD-L1 IPs derived from MDA-MB-231 cells transfected with control siRNA or siRNAs targeting the indicated HDACs. **f**, IB analysis of WCL and anti-PD-L1 IPs derived from MDA-MB-231 cells transduced with shRNAs against *HDAC2* or GFP. **g**, IB analysis of WCL and anti-PD-L1 IPs derived from MDA-MB-231 WT or *HDAC2*-KO cells. **h**, IB analysis of WCL and anti-PD-L1 IPs derived from MDA-MB-231 cells treated with the indicated HDAC inhibitors (santacruzamate A (SCA), 20 μM; ACY1215, 40 μM; ACY957, 20 μM) for 3 h. **i**, IB analysis of WCL and anti-PD-L1 IPs derived from MDA-MB-231 WT or *HDAC2*-KO cells, treated with or without 50 μM HDAC2 inhibitor (HDAC2i) for 4 h. For the western blots in **a–i**, $n=2$ independent experiments were performed with similar results. Source data are available online.

(Fig. 6e and Extended Data Fig. 5k–m), supporting the idea that Lys263 acetylation might inhibit PD-L1 nuclear localization to potentially impact gene transcription. Conceivably, highly expressed PD-L1 in tumour cells may subsequently transactivate a cohort of genes of the IFN, NF- κ B and MHC I pathways, leading to a relatively high response to PD-L1/PD-1 blockade in clinical studies^{9,39}.

To dissect the nuclear roles of PD-L1 in regulating gene expression, we performed chromatin immunoprecipitation coupled with ultra-high-throughput DNA sequencing (ChIP-seq) analysis using MDA-MB-231 CD274-KO cells in which we reintroduced HA-tagged PD-L1. Notably, we observed an overlap of more than 60% between PD-L1 ChIP-seq peak genes and differentially expressed genes



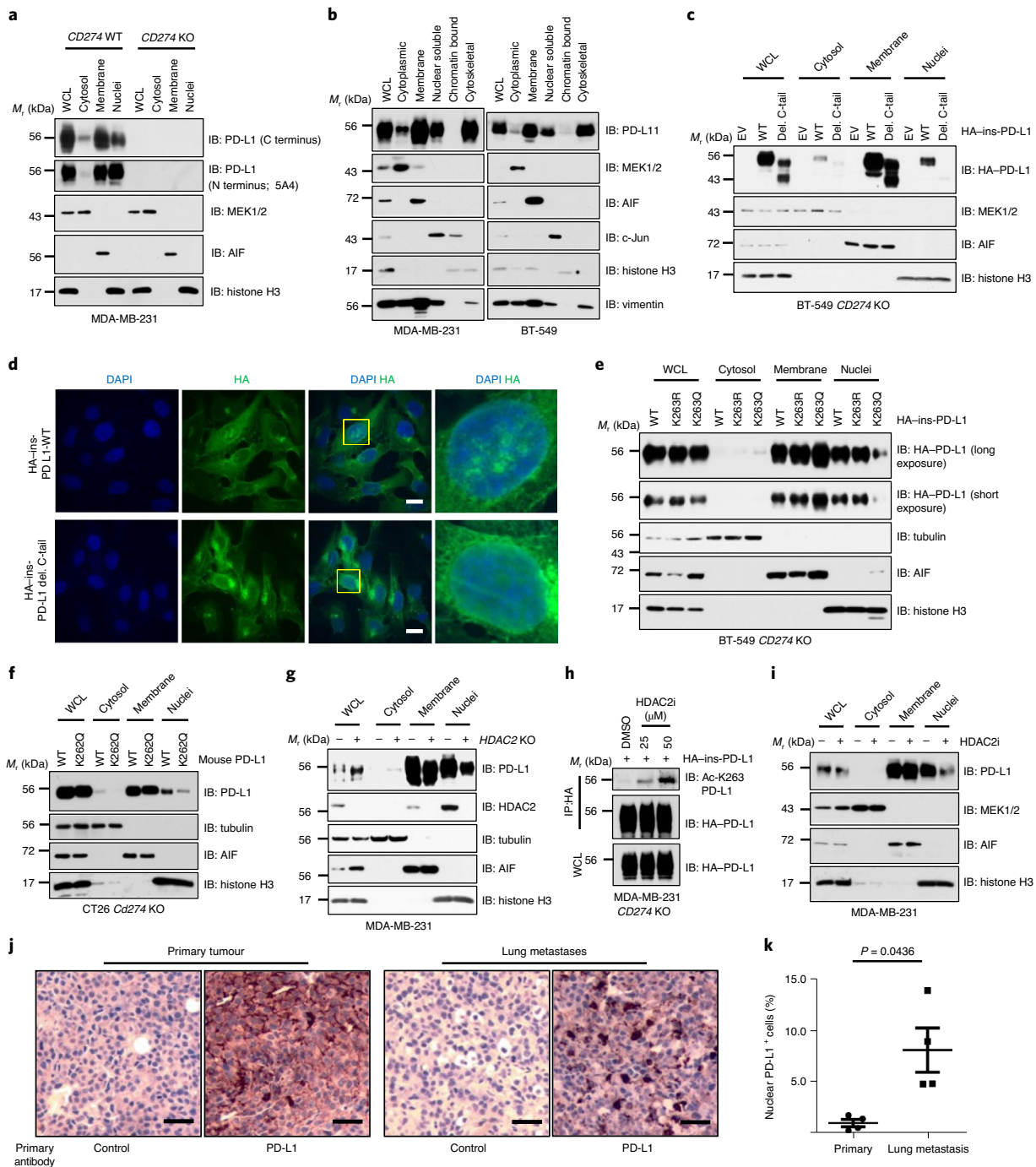


Fig. 3 | Nuclear translocation of PD-L1 is regulated by acetylation of Lys 263. **a**, IB analysis of WCL, cytosol, membrane and nuclear fractions derived from MDA-MB-231 WT or CD274-KO cells, purified using a Cell Signaling Technology kit. **b**, IB analysis of the WCL, cytoplasmic, membrane, nuclear soluble, chromatin-bound and cytoskeletal fractions derived from MDA-MB-231 and BT-549 cells, purified using a Thermo Fisher Scientific kit. **c**, Fractionation analysis for PD-L1 in BT-549 CD274-KO cells transfected with HA-ins-PD-L1 WT or C-tail deletion (del. C-tail) mutant. **d**, Immunofluorescence (IF) with anti-HA antibody and 4,6-diamidino-2-phenylindole (DAPI) staining of MDA-MB-231 CD274-KO cells transduced with HA-ins-PD-L1 WT or the C-tail deletion mutant lentivirus. The areas indicated by the yellow boxes are magnified on the right (final magnification, 100×). $n=2$ independent experiments were performed with similar results. Scale bars, 10 μm. **e**, Fractionation analysis for PD-L1 in BT-549 CD274-KO cells transfected with the indicated constructs. **f**, Fractionation analysis for mouse WT PD-L1 or PD-L1^{K262Q} (corresponding to K263Q for human PD-L1) mutant re-expressed in CT26 Cd274-KO cells. **g**, IB analysis of WCL, cytosol, membrane and nuclear fractions derived from MDA-MB-231 WT or HDAC2-KO cells. **h**, IB analysis of WCL and anti-HA IPs derived from MDA-MB-231 CD274-KO cells transduced with HA-ins-PD-L1 lentivirus. The resulting cells were treated with DMSO or the indicated concentration of HDAC2 inhibitor (HDAC2i) for 4 h. **i**, Fractionation analysis for PD-L1 in MDA-MB-231 cells treated with 50 μM HDAC2 inhibitor for 6 h. **j**, Immunohistochemistry analysis of mouse PD-L1 expression and localization in B16F10 primary tumours (subcutaneous injection) and lung metastases (tail vein injection). Scale bars, 50 μm, ×20 magnification. **k**, Quantification of PD-L1 nuclear-positive cell rates in **j**. Data are mean ± s.e.m.; $n=4$ mice. The P value was calculated using a two-tailed Student's *t*-test with Welch's correction. For the western blots in **a–e** and **g–i**, $n=2$ independent experiments were performed with similar results. Source data are available online.

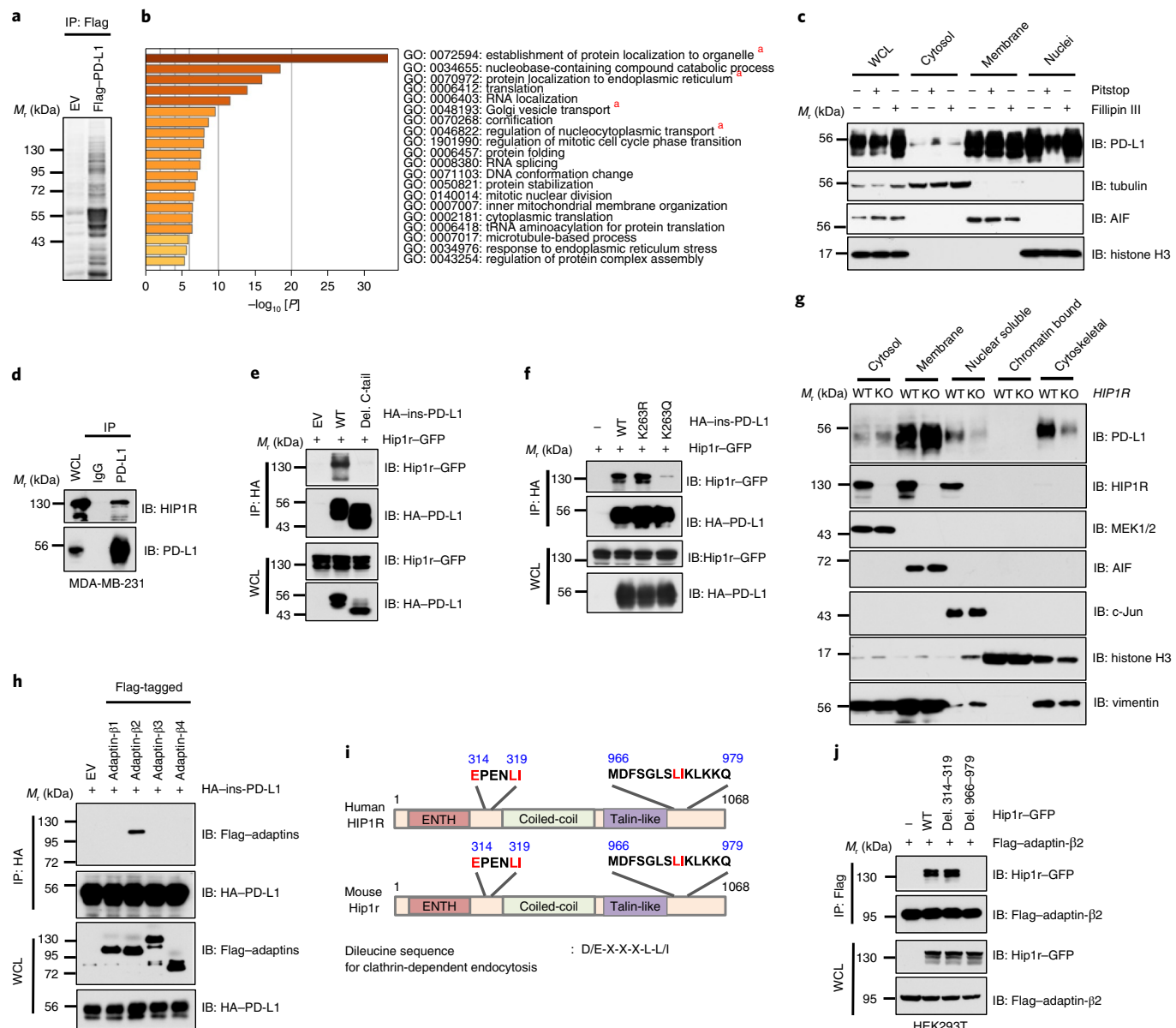


Fig. 4 | PD-L1 interacts with HIP1R to engage clathrin-dependent endocytosis. **a**, Anti-Flag immunoprecipitation coupled with MS analysis was used to identify PD-L1-interacting proteins in HEK293T cells. *n* = 2 biologically independent experiments. **b**, The results from the MS analysis in **a** were analysed for GO term enrichment. The red asterisks denote pathways that are associated with protein translocation. *n* = 2 independent experiments with similar results. *P* values were calculated using hypergeometric tests. **c**, MDA-MB-231 cells were treated with 5 μM Pitstop or 10 μg ml⁻¹ Fillipin III for 15 min, and then analysed using fractionation. **d**, IB analysis of WCL and anti-PD-L1 IPs derived from MDA-MB-231 cells. **e**, IB analysis of WCL and anti-HA IPs derived from HEK293T cells transfected with mouse Hip1r-GFP and HA-ins-PD-L1 WT or C-tail deletion mutant. **f**, IB analysis of WCL and anti-HA IPs derived from HEK293T cells transfected with mouse Hip1r-GFP and HA-ins-PD-L1 WT, K263R or K263Q. **g**, Fractionation analysis for PD-L1 in MDA-MB-231 WT or HIP1R-KO cells. **h**, IB analysis of WCL and anti-HA IPs derived from HEK293T cells transfected with HA-ins-PD-L1 and the indicated adaptin constructs. **i**, Schematic of the human and mouse HIP1R protein domains and candidate dileucine sequences. **j**, IB analysis of WCL and anti-Flag IPs derived from HEK293T cells transfected with Flag-tagged adaptin β2 (AP2B1) and the indicated dileucine-sequence-deleted constructs. For the western blots in **c-h** and **j**, *n* = 2 independent experiments were performed with similar results. Source data are available online.

in CD274-KO cells on the basis of RNA-seq analysis (Fig. 6f–i). Moreover, we found that genes that were identified to be downregulated in CD274-KO cells, such as NF-κB-signalling-related genes, possess PD-L1-binding peaks on the basis of ChIP-seq analysis (Fig. 6j). This result suggests a model in which nuclear PD-L1 might specifically trigger gene expression involved in immune-response pathways to modulate the anti-tumour immune response. In support of this notion, we identified a subset of de novo PD-L1-specific binding motifs and canonical DNA-binding motifs of various

transcription factors (Fig. 6k, and Supplementary Tables 6 and 7). Comparing DNA-binding patterns with other transcription factors, we found a positive correlation with some transcription factors that are related to immune response, such as STAT3, RelA/p65 and c-Jun⁴⁰ (Extended Data Fig. 5n). Indeed, PD-L1 could interact with RelA and IFN-regulatory factor (IRF) proteins (Extended Data Fig. 5o–q), indicating that PD-L1 can probably interact with transcription factors on DNA to affect transcription events that are involved in anti-tumour immunity.

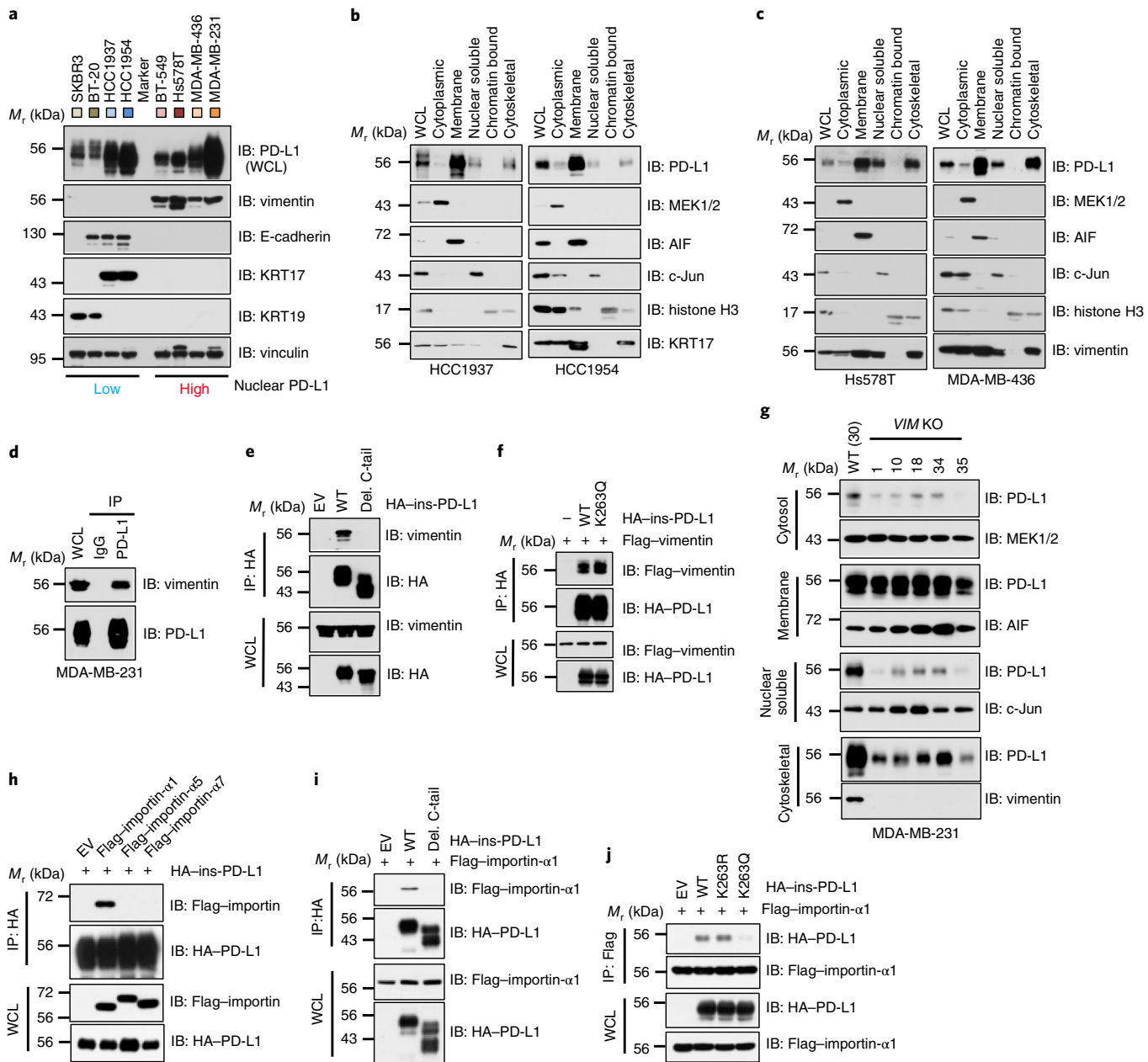
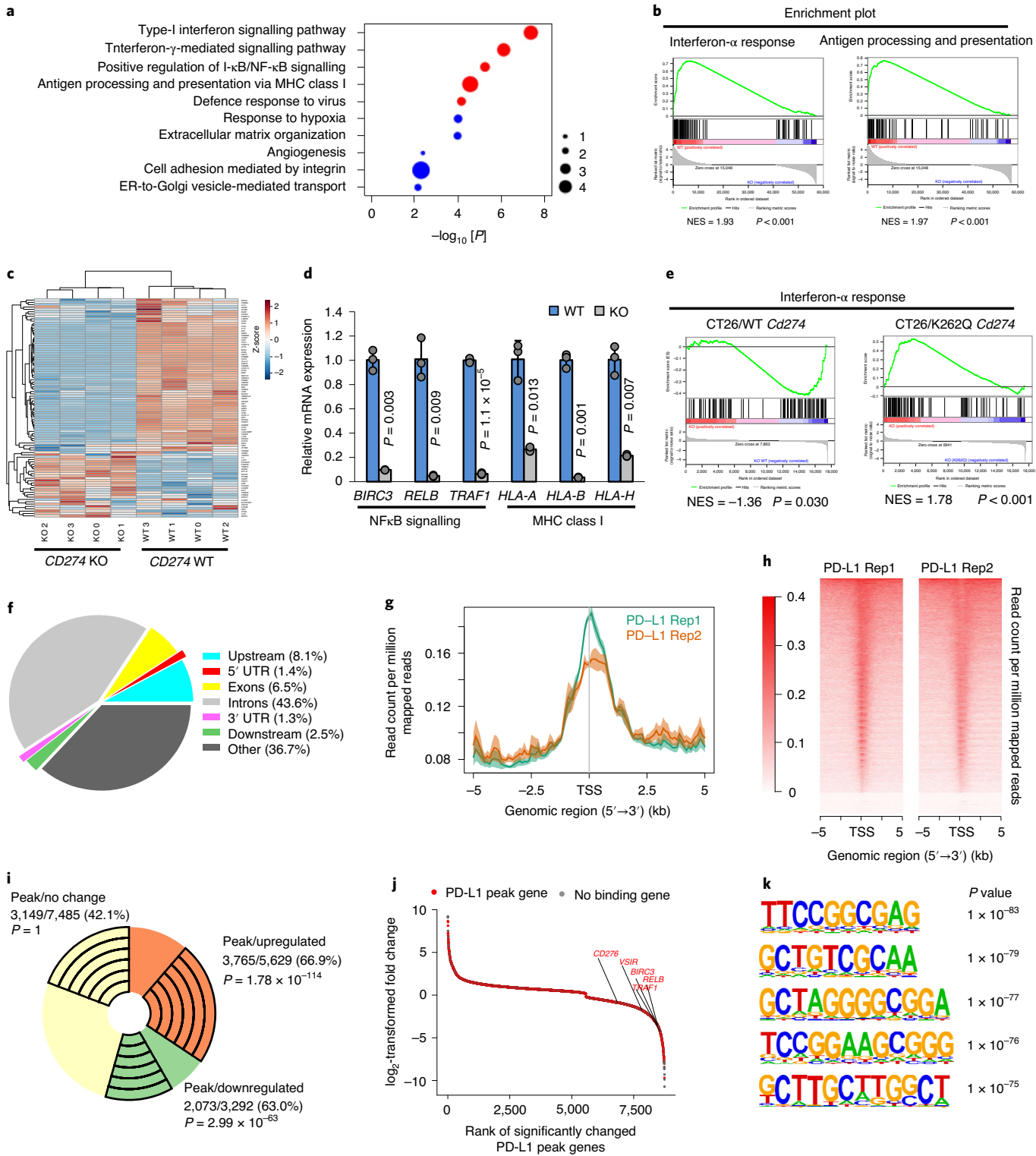


Fig. 5 | The PD-L1 nuclear-translocation process requires vimentin and importin- α 1. **a**, IB analysis of WCL derived from a panel of breast cancer cell lines with differently expressed cytoskeletal proteins. **b**, Fractionation analysis (using a kit from Thermo Fisher Scientific) of PD-L1 from vimentin^{low} breast cancer cell lines, HCC1937 and HCC1954. **c**, Fractionation analysis for PD-L1 expression in vimentin^{high} breast cancer cell lines, Hs578T and MDA-MB-436. **d**, IB analysis of WCL and anti-PD-L1 IPs derived from MDA-MB-231 cells transduced with HA-ins-PD-L1 WT or C-tail deletion mutant virus. **e**, IB analysis of WCL and anti-HA IPs derived from HEK293T cells transfected with Flag-tagged vimentin and HA-ins-PD-L1 WT or K263Q mutant construct. **f**, IB analysis of WCL and anti-HA IPs derived from HEK293T cells transfected with Flag-tagged vimentin and HA-ins-PD-L1 WT or K263R mutant construct. **g**, Fractionation analysis for PD-L1 in MDA-MB-231 WT (clone 30) or VIM-KO single-cell clones (clones 1, 10, 18, 34 and 35). **h**, IB analysis of WCL and anti-HA IPs derived from HEK293T cells transfected with HA-ins-PD-L1 and the indicated Flag-tagged importin constructs. **i**, IB analysis of WCL anti-HA IPs derived from HEK293T cells transfected with Flag-importin- α 1 (IPOA1/KPNA2) and the indicated HA-ins-PD-L1 WT or C-tail deletion construct. **j**, IB analysis of WCL anti-Flag IPs derived from HEK293T cells transfected with Flag-importin- α 1 and the indicated HA-ins-PD-L1 WT, K263R or K263Q mutant construct. For the western blots in **a–j**, $n=2$ independent experiments were performed with similar results. Source data are available online.

Thus, our findings suggest a model that underlies how PD-L1 expression correlates with the ‘cold tumour’ versus ‘warm tumour’ in response to PD-1 blockade. First, highly expressed PD-L1 on the plasma membrane engages PD-1 on T cells to suppress T-cell activation; second, PD-L1 in the nucleus enhances the activation of multiple immune-response pathways to build up a positive feedback

loop of increased PD-L1 expression to foster the evasion of immune surveillance. By contrast, nuclear PD-L1 also stimulates the inflammation pathway and increases neoantigen presentation, which might contribute to the observed responsiveness to anti-PD-1/PD-L1 treatment in patients with high PD-L1 expression (Extended Data Fig. 5r).



Blocking PD-L1 nuclear translocation enhances PD-1 blockade therapy. Unexpectedly, aside from these inflammation-stimulating aspects of PD-L1 functions, our RNA-seq data show that several immune checkpoint genes, such as *PDCD1LG2* (encoding PD-L2), *VSIR* (encoding VISTA) and *CD276* (encoding B7-H3) were also downregulated by *CD274* depletion (Fig. 7a). These results were validated using RT-qPCR and western blot analyses in *CD274*-KO and -knockdown cells (Fig. 7b-d and Extended Data Fig. 6a-d). Especially, *PDCD1LG2* and *VSIR* expression was positively correlated

with *CD274* expression in human breast cancer cells (Extended Data Fig. 6e-g). As PD-L2, VISTA and B7-H3 are also involved in the evasion of immune surveillance¹¹, our findings suggest that nuclear PD-L1 could potentially upregulate these immune checkpoint genes in tumour cells to acquire resistance to PD-L1/PD-1 blockade.

On the basis of our findings that HDAC2 triggers the nuclear translocation of PD-L1 to alter gene transcription, we hypothesize that pharmacological inhibition of HDAC2 would reduce nuclear PD-L1 and might represent a potential strategy for enhancing the

efficacy of PD-1-blockade-based immunotherapy. Bioinformatics database analysis showed that HDAC2 mRNA was increased in various tumours compared with normal tissues (Extended Data Fig. 6h). Higher HDAC2 or vimentin level was correlated with poor overall survival rates and a potential worse response for PD-1 antibody therapy (Extended Data Fig. 6i–k). Moreover, treatment with HDAC2 inhibitor could also induce IFN-type-III-related genes, *IFNL2* (which encodes IL28A) and *IFNL3* (which encodes IL28B), resulting in STAT1 stimulation (Extended Data Fig. 6l,m). HDAC2 inhibition did not alter the expression of endogenous retroviral genes. However, the double-stranded-RNA pathogen-recognition-receptor-related genes as well as MHC class-I antigen presenting genes were significantly increased (Extended Data Fig. 6n–p), suggesting that HDAC2 inhibition might induce a microenvironment with high infiltrating immune cells to improve the responsiveness to PD-1 blockade (Extended Data Fig. 6q).

Pharmacologic inhibition of HDAC2 might synergize with PD-1/PD-L1 blockade for cancer treatment; we therefore examined this hypothesis using the MC38 syngeneic mouse tumour model treated with anti-PD-1 antibodies and/or HDAC2 inhibitor. Notably, compared with the anti-PD-1 treatment group, combination of HDAC2 inhibitor and anti-PD-1 antibodies substantially slowed tumour growth and increased the survival rate (Fig. 7e,f). However, the therapeutic benefit of combination treatment was not observed in immunocompromized nude mice (Extended Data Fig. 7a,b), supporting the notion that the anti-tumour effect depends on T cells. We next evaluated tumour-infiltrating lymphocytes (TILs) in tumours and found significantly increased proportions of CD8⁺ and CD8⁺Gran B (granzyme B)⁺, but not CD4⁺ or CD4⁺FOXP3⁺, T cells out of CD45⁺CD3⁺ TILs in the combined treatment group (Fig. 7g,h). Notably, the ratio of CD8⁺ T cells to regulatory T cells (CD4⁺FOXP3⁺), which is a potential predictor of response to immunotherapy, was also increased in the combination-treatment group (Fig. 7i). Among various cytokines, TNF α was reduced in the HDAC-inhibitor treatment group but retained at a relatively moderate level in the combination-treatment group (Fig. 7j and Extended Data Fig. 7c). These findings are consistent with recent reports that blocking TNF α could overcome resistance to immunotherapy^{42,43}. Interestingly, PD-1 antibody treatment increased nuclear PD-L1 signal, which was somehow attenuated after the combined treatment with HDAC2 inhibitor; however, the underlying mechanism remains to be elucidated (Extended Data Fig. 7d).

To further examine the role of acetylation in PD-L1 functions, we compared the sensitivity to PD-1/PD-L1 blockade between *Cd274* WT and *Cd274*^{K262Q} mutant in the CT26 syngeneic tumour model. Strikingly, the mice expressing *Cd274*^{K262Q} showed a better response and improved survival after treatment with anti-PD-1 antibodies

compared with the WT group (Extended Data Fig. 7e,f). Moreover, the enhanced therapeutic effects in MC38 *Cd274*^{K262Q} could not be observed in the combined treatment group (Fig. 7k and Extended Data Fig. 7g), suggesting that an acetylation-dependent PD-L1 translocation confers therapeutic benefit of the combined treatment.

Discussion

Independent of its immune-suppressive function on the plasma membrane, PD-L1 was shown to endow tumour cells with anti-apoptotic ability⁴⁴, promote mTOR activity and regulate glycolytic metabolism⁴⁵. Here we demonstrate that a portion of PD-L1 translocates into the nucleus to regulate the expression of pro-inflammatory and immune-response-related genes, suggesting that transcriptional regulation by PD-L1 might foster immune inflammation in the local tumour microenvironment to render the tumour more sensitive to immune checkpoint blockade therapy. Our findings explain why high PD-L1 levels predict a better response to PD-1 blockade, as found in clinical trials⁴⁶. Moreover, we found that the nuclear function of PD-L1 is controlled by Lys 263 acetylation in the C-tail. Notably, nuclear PD-L1 is enriched in lung metastatic tumours, suggesting that there is a potential interplay between tumour aggressiveness and PD-L1 translocation. Further studies to clarify how nuclear PD-L1 could contribute to distant metastasis of cancer are warranted.

Surprisingly, nuclear PD-L1 also triggers expression of other immune checkpoint molecules that are not targeted by PD-1/PD-L1 blockade, leading to possible acquired immunotherapy resistance (Extended Data Fig. 7h). Blocking the nuclear translocation of PD-L1 with HDAC2 inhibitor might therefore potentially decrease transcription of these immune checkpoint genes, resulting in increased CD8⁺ cytotoxic T-cell infiltration and decreased TNF α levels in tumours, which in turn augments the anti-tumour immune response triggered by therapeutic antibodies against PD-1. Thus, our studies provide a molecular mechanism and rationale for combining HDAC2 inhibition with PD-1/PD-L1 blockade as an effective immunotherapy for cancer.

Online content

Any methods, additional references, Nature Research reporting summaries, source data, extended data, supplementary information, acknowledgements, peer review information; details of author contributions and competing interests; and statements of data and code availability are available at <https://doi.org/10.1038/s41556-020-0562-4>.

Received: 19 August 2019; Accepted: 21 July 2020;

Published online: 24 August 2020

Fig. 6 | Nuclear PD-L1 regulates the gene expression of immune-response and regulatory pathways. **a**, The top 10 enriched GO (biological process) terms of downregulated genes ($n=3,292$) after *CD274* KO in MDA-MB-231 cells. $n=4$ biologically independent sequenced samples per group. Statistical analysis was performed using modified Fisher's exact tests with Benjamini-Hochberg correction. Immune-response-related terms are indicated in red. The dot size indicates the fold enrichment. ER, endoplasmic reticulum. **b**, Downregulated gene-set enrichment analysis (GSEA) signatures after *CD274* KO in MDA-MB-231 cells. $n=4$ biologically independent sequenced samples per group. P values were calculated using Kolmogorov-Smirnov tests. NES, normalized enrichment score. **c**, Heat map of the IFN α genes in MDA-MB-231 WT and *CD274*-KO cells. Data are mean \pm s.d. of $n=3$ independent experiments. P values were calculated using two-tailed Student's *t*-tests. **d**, RT-qPCR analysis of the indicated genes from MDA-MB-231 WT and *CD274*-KO cells. **e**, GSEA signatures of 'Interferon α response' after re-expressing mouse WT or K262Q-mutant *Cd274* in *Cd274*-KO CT26 cells. $n=3$ biologically independent sequenced samples per group. Statistical analysis was performed using Kolmogorov-Smirnov tests. **f**, The genomic distribution of HA-tag ChIP-seq peaks in MDA-MB-231 *CD274*-KO cells expressing HA-tagged PD-L1. **g**, PD-L1 ChIP-seq signal height and position relative to transcription start sites (TSS) for all genes in MDA-MB-231 cells. Two replicates are shown. The lines show the average profile of genes. The shading indicates the s.e. of all human hg38 genes. $n=58,713$. **h**, ChIP-seq density heat map of PD-L1 enrichment in MDA-MB-231 cells, within 5 kb around TSS. Gene order was arranged from highest to lowest density. **i**, The fraction of genes with PD-L1 peaks among upregulated, downregulated or no-change genes after *CD274* KO in MDA-MB-231 cells. The exact numbers of genes, percentage and P values (calculated using hypergeometric tests) in each group are shown. **j**, Rank-ordered depiction of the \log_2 -transformed fold change for each significantly changed gene after *CD274* KO. The 5,838 genes that have PD-L1 binding peaks are indicated in red. Grey dots indicate genes that have no PD-L1 binding. **k**, The top-enriched motifs at the PD-L1-binding sites ($n=50,738$) in MDA-MB-231 cells. P values were calculated using hypergeometric distributions. Source data are available online.

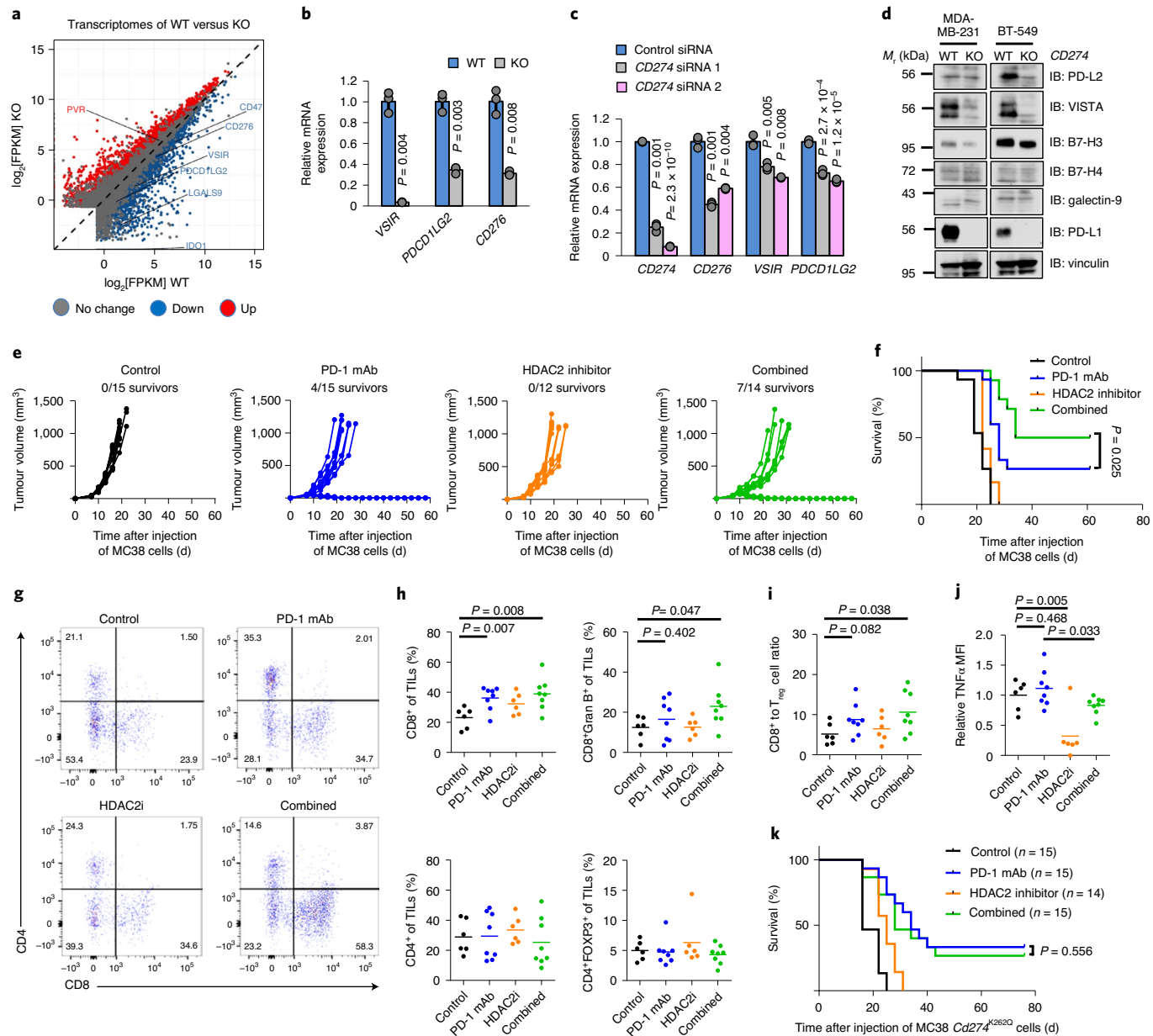


Fig. 7 | Nuclear PD-L1 regulates the gene expression of immune-response and regulatory pathways to influence the efficacy of anti-PD-1 immunotherapy.

a, The transcriptome of MDA-MB-231 cells after CD274 KO. FPKM, fragments per kilobase of transcript per million mapped reads. **b**, RT-qPCR analysis of the indicated genes from MDA-MB-231 WT or CD274-KO cells. Data are mean \pm s.d. of $n=3$ independent experiments. **c**, RT-qPCR analysis of the indicated genes from MDA-MB-231 cells transfected with control siRNA or siRNA against CD274. Data are mean \pm s.d. of $n=3$ independent experiments. **d**, IB analysis of WCL derived from WT or CD274-KO MDA-MB-231 and BT-549 cells. The western blots were performed for $n=2$ independent experiments with similar results. **e**, Volumes of MC38 syngeneic tumours treated with control antibodies (black lines; $n=15$), anti-PD-1 monoclonal antibodies (mAb) (blue lines; $n=15$), the HDAC2 inhibitor santacruzamate A (orange lines; $n=12$) or combined therapy (green lines; $n=14$) were plotted individually. **f**, Kaplan-Meier survival curves for each treatment group (control, $n=15$; PD-1 monoclonal antibodies, $n=15$; HDAC2i, $n=12$; combined, $n=14$). The P value was calculated using a two-sided Gehan-Breslow-Wilcoxon test. **g**, Representative dot plots of CD4⁺ and CD8⁺ TILs in MC38 syngeneic tumours. **h**, The proportions of CD8⁺, CD8⁺ Gran B⁺, CD4⁺ and CD4⁺FOXP3⁺ T cells out of CD45⁺CD3⁺ TILs in MC38 syngeneic tumours treated with control antibodies ($n=6$), anti-PD-1 monoclonal antibodies ($n=8$), HDAC2 inhibitor ($n=6$) or combined therapy ($n=8$). **i**, The ratio of CD8⁺ T cells to regulatory T (T_{reg}) cells (CD4⁺FOXP3⁺) in the treated MC38 tumours from **g** was calculated. **j**, TILs from treated MC38 tumours from **h** were incubated with a cell-stimulation cocktail for 4 h, and expression levels of TNF α were examined. MFI, mean fluorescence intensity. **k**, Survival curves of MC38-Cd274^{K262Q} tumour-bearing C57BL/6 mice that were treated as indicated. P values were calculated using two-sided Gehan-Breslow-Wilcoxon tests. For **b**, **c** and **h-j**, P values were calculated using two-tailed Student's *t*-tests. Each circle in **h-j** represents a single tumour, shown with the mean value of each group. Source data are available online.

References

- Chen, D. S. & Mellman, I. Elements of cancer immunity and the cancer-immune set point. *Nature* **541**, 321–330 (2017).
- Baumeister, S. H., Freeman, G. J., Dranoff, G. & Sharpe, A. H. Coinhibitory pathways in immunotherapy for cancer. *Annu. Rev. Immunol.* **34**, 539–573 (2016).

3. Ribas, A. & Wolchok, J. D. Cancer immunotherapy using checkpoint blockade. *Science* **359**, 1350–1355 (2018).
4. Sharma, P., Hu-Lieskovian, S., Wargo, J. A. & Ribas, A. Primary, adaptive, and acquired resistance to cancer immunotherapy. *Cell* **168**, 707–723 (2017).
5. Restifo, N. P., Smyth, M. J. & Snyder, A. Acquired resistance to immunotherapy and future challenges. *Nat. Rev. Cancer* **16**, 121–126 (2016).
6. Zhang, J. et al. Cyclin D-CDK4 kinase destabilizes PD-L1 via cullin 3-SPOP to control cancer immune surveillance. *Nature* **553**, 91–95 (2018).
7. Lim, S. O. et al. Deubiquitination and stabilization of PD-L1 by CSN5. *Cancer Cell* **30**, 925–939 (2016).
8. Zhang, J., Dang, F., Ren, J. & Wei, W. Biochemical aspects of PD-L1 regulation in cancer immunotherapy. *Trends Biochem. Sci.* **43**, 1014–1032 (2018).
9. Galluzzi, L., Chan, T. A., Kroemer, G., Wolchok, J. D. & Lopez-Soto, A. The hallmarks of successful anticancer immunotherapy. *Sci. Transl. Med.* **10**, eaat7807 (2018).
10. Ansell, S. M. et al. PD-1 blockade with nivolumab in relapsed or refractory Hodgkin's lymphoma. *N. Engl. J. Med.* **372**, 311–319 (2015).
11. Inuzuka, H. et al. Acetylation-dependent regulation of Skp2 function. *Cell* **150**, 179–193 (2012).
12. Nihira, N. T. et al. Acetylation-dependent regulation of MDM2 E3 ligase activity dictates its oncogenic function. *Sci. Signal.* **10**, eaai8026 (2017).
13. Song, H. et al. Acetylation of EGF receptor contributes to tumor cell resistance to histone deacetylase inhibitors. *Biochem. Biophys. Res. Commun.* **404**, 68–73 (2011).
14. Lin, S. Y. et al. Nuclear localization of EGF receptor and its potential new role as a transcription factor. *Nat. Cell Biol.* **3**, 802–808 (2001).
15. Gao, Y. S., Hubbert, C. C. & Yao, T. P. The microtubule-associated histone deacetylase 6 (HDAC6) regulates epidermal growth factor receptor (EGFR) endocytic trafficking and degradation. *J. Biol. Chem.* **285**, 11219–11226 (2010).
16. Li, C. W. et al. Glycosylation and stabilization of programmed death ligand-1 suppresses T-cell activity. *Nat. Commun.* **7**, 12632 (2016).
17. Mezzadra, R. et al. Identification of CMTM6 and CMTM4 as PD-L1 protein regulators. *Nature* **549**, 106–110 (2017).
18. Horita, H., Law, A., Hong, S. & Middleton, K. Identifying regulatory posttranslational modifications of PD-L1: a focus on monoubiquitinon. *Neoplasia* **19**, 346–353 (2017).
19. Lasko, L. M. et al. Discovery of a selective catalytic p300/CBP inhibitor that targets lineage-specific tumours. *Nature* **550**, 128–132 (2017).
20. Glozak, M. A., Sengupta, N., Zhang, X. & Seto, E. Acetylation and deacetylation of non-histone proteins. *Gene* **363**, 15–23 (2005).
21. Pavlik, C. M. et al. Santacruzamate A, a potent and selective histone deacetylase inhibitor from the Panamanian marine cyanobacterium cf. *Symploca* sp. *J. Nat. Prod.* **76**, 2026–2033 (2013).
22. von Kleist, L. et al. Role of the clathrin terminal domain in regulating coated pit dynamics revealed by small molecule inhibition. *Cell* **146**, 471–484 (2011).
23. Schnitzer, J. E., Oh, P., Pinney, E. & Allard, J. Filipin-sensitive caveolae-mediated transport in endothelium: reduced transcytosis, scavenger endocytosis, and capillary permeability of select macromolecules. *J. Cell Biol.* **127**, 1217–1232 (1994).
24. McMahon, H. T. & Boucrot, E. Molecular mechanism and physiological functions of clathrin-mediated endocytosis. *Nat. Rev. Mol. Cell Biol.* **12**, 517–533 (2011).
25. Bonifacino, J. S. & Traub, L. M. Signals for sorting of transmembrane proteins to endosomes and lysosomes. *Annu. Rev. Biochem.* **72**, 395–447 (2003).
26. Wang, H. et al. HIP1R targets PD-L1 to lysosomal degradation to alter T cell-mediated cytotoxicity. *Nat. Chem. Biol.* **15**, 42–50 (2019).
27. Paczkowski, J. E., Richardson, B. C. & Fromme, J. C. Cargo adaptors: structures illuminate mechanisms regulating vesicle biogenesis. *Trends Cell Biol.* **25**, 408–416 (2015).
28. Mattera, R., Boehm, M., Chaudhuri, R., Prabhu, Y. & Bonifacino, J. S. Conservation and diversification of dileucine signal recognition by adaptor protein (AP) complex variants. *J. Biol. Chem.* **286**, 2022–2030 (2011).
29. Fazal, F., Minhajuddin, M., Bijli, K. M., McGrath, J. L. & Rahman, A. Evidence for actin cytoskeleton-dependent and -independent pathways for RelA/p65 nuclear translocation in endothelial cells. *J. Biol. Chem.* **282**, 3940–3950 (2007).
30. Cortes-Reynosa, P., Robledo, T. & Salazar, E. P. Epidermal growth factor promotes epidermal growth factor receptor nuclear accumulation by a pathway dependent on cytoskeleton integrity in human breast cancer cells. *Arch. Med. Res.* **40**, 331–338 (2009).
31. Elosegui-Artola, A. et al. Force triggers YAP nuclear entry by regulating transport across nuclear pores. *Cell* **171**, 1397–1410 (2017).
32. Satelli, A. et al. Potential role of nuclear PD-L1 expression in cell-surface vimentin positive circulating tumor cells as a prognostic marker in cancer patients. *Sci. Rep.* **6**, 28910 (2016).
33. Yu, Y. et al. Cancer-associated fibroblasts induce epithelial-mesenchymal transition of breast cancer cells through paracrine TGF- β signalling. *Br. J. Cancer* **110**, 724–732 (2014).
34. Goldfarb, D. S., Corbett, A. H., Mason, D. A., Harreman, M. T. & Adam, S. A. Importin alpha: a multipurpose nuclear-transport receptor. *Trends Cell Biol.* **14**, 505–514 (2004).
35. Wagstaff, K. M., Sivakumaran, H., Heaton, S. M., Harrich, D. & Jans, D. A. Ivermectin is a specific inhibitor of importin α/β -mediated nuclear import to inhibit replication of HIV-1 and dengue virus. *Biochem. J.* **443**, 851–856 (2012).
36. Isokane, M. et al. Plasma-membrane-anchored growth factor pro-amphiregulin binds A-type lamin and regulates global transcription. *J. Cell Sci.* **121**, 3608–3618 (2008).
37. Hancock, M. L. et al. Insulin receptor associates with promoters genome-wide and regulates gene expression. *Cell* **177**, 722–736 (2019).
38. Tu, X. et al. PD-L1 (B7-H1) competes with the RNA exosome to regulate the DNA damage response and can be targeted to sensitize to radiation or chemotherapy. *Mol. Cell* **74**, 1215–1226 (2019).
39. Zou, W., Wolchok, J. D. & Chen, L. PD-L1 (B7-H1) and PD-1 pathway blockade for cancer therapy: mechanisms, response biomarkers, and combinations. *Sci. Transl. Med.* **8**, 328rv324 (2016).
40. He, G. & Karin, M. NF-kappaB and STAT3—key players in liver inflammation and cancer. *Cell Res.* **21**, 159–168 (2011).
41. Ceeraz, S., Nowak, E. C. & Noelle, R. J. B7 family checkpoint regulators in immune regulation and disease. *Trends Immunol.* **34**, 556–563 (2013).
42. Bertrand, F. et al. TNFalpha-blockade overcomes resistance to anti-PD-1 in experimental melanoma. *Nat. Commun.* **8**, 2256 (2017).
43. Perez-Ruiz, E. et al. Prophylactic TNF blockade uncouples efficacy and toxicity in dual CTLA-4 and PD-1 immunotherapy. *Nature* **569**, 428–432 (2019).
44. Azuma, T. et al. B7-H1 is a ubiquitous antiapoptotic receptor on cancer cells. *Blood* **111**, 3635–3643 (2008).
45. Chang, C. H. et al. Metabolic competition in the tumor microenvironment is a driver of cancer progression. *Cell* **162**, 1229–1241 (2015).
46. Patel, S. P. & Kurzrock, R. PD-L1 expression as a predictive biomarker in cancer immunotherapy. *Mol. Cancer Ther.* **14**, 847–856 (2015).

Publisher's note Springer Nature remains neutral with regard to jurisdictional claims in published maps and institutional affiliations.

© The Author(s), under exclusive licence to Springer Nature Limited 2020

Methods

Cell culture, transfection, virus infection and treatments. HEK293T, Hs578T, MDA-MB-231, MDA-MB-436, A375, SW839, RAW264.7, MEF, B16F10, MCF7, MDA-MB-468, SKBR3, BT-20, T47D and MC38 cells were cultured in DMEM medium. BT-549, HCC1937, HCC1954, DU145, ZR-75-1 and CT26 cells were cultured in RPMI 1640 medium. All medium contained 10% FBS, 100 U penicillin and 100 µg ml⁻¹ streptomycin. A summary of the source information and authentication status of all of the cell lines is provided in Supplementary Table 8. For the BT-20 line, although some stocks have previously been shown to be misidentified⁴⁷, we performed STR analysis, and the ATCC certification report in the Extended Data Fig. 1b demonstrates that the BT-20 line that we used in this study is not cross-contaminated. MDA-MB-231 CD274-KO cells and BT549 CD274-KO cells were a gift from M.-C. Hung. Transfection was performed using PEI (Polysciences) or Lipofectamine (Thermo Fisher Scientific). For lentiviral infection, HEK293T cells were transfected with packaging vectors (delta-8.9 and VSVG) and GFP shRNA, CD274 shRNA, HDAC2 shRNA, EP300 shRNA pLKO plasmids, or pLenti-HA-ins-PD-L1 WT or its C-tail-deletion-mutant plasmids; the virus particles were then collected for infection. Cells were selected with puromycin or hygromycin. Silencer Select Negative Control No. 2 siRNA, HDAC6 siRNA (M-003499-00-0005) and CD274-specific siRNAs (s26547 and s26548) were purchased from Dharmacon/Horizon Discovery. HDAC3 siRNA (sc-35538) was obtained from Santa Cruz Biotechnology. HDAC1 (Hs01_00142115) and HDAC2 (Hs01_00079968) siRNAs were purchased from Merck. Transfection of siRNAs was performed using Lipofectamine RNAi MAX (Thermo Fisher Scientific). For TGFβ1 treatment, cells cultured in 1% FBS were treated with 10 ng ml⁻¹ recombinant human TGFβ1 (BioLegend). Cycloheximide assays were performed as described previously⁴⁸. MG-132 (MBL-PI102) and tunicamycin (T7765) were purchased from Enzo Life Sciences and Sigma-Aldrich, respectively. Cycloheximide (AC357420050) was purchased from Thermo Fisher Scientific. Santacruzamate A (S7595) and ivermectin (S1351) were purchased from Selleckchem. A485 (6387) was purchased from Tocris. ACY957 and ACY1215 were provided by Acetylon Pharmaceuticals. Filipin III (F4767) and Pitstop (ab120685) were purchased from Merck and Abcam, respectively.

Plasmids. Importin-α1, -α5 and -α7, SIRT, HDAC and IRF cDNA were amplified and cloned into pcDNA3-Flag vector as previously described^{11,12}. CREBBP, EP300, GCN5, PCAF and KAT5 (which encodes Tip60) cDNA were amplified and cloned into the pcDNA3-HA vector. Mouse Hip1r-GFP and Halo-tag vectors were obtained from Addgene. C-terminal, Myc-tagged PD-L1 and glycosylation-deficient 4NQ (N35Q, N192Q, N200Q and N219Q) mutant PD-L1 were gifts from M.-C. Hung. cDNA encoding adaptin-β1, -β2, -β3 and -β4 were provided by K. Nakayama and J. S. Bonifacino. cDNA encoding the C-terminal domain of PD-L1 (amino acids 260–290) was amplified and subcloned into the CMV-GST vector. To generate N-terminal HA-tag-inserted PD-L1, HA sequences were inserted after signal peptide sequence within full-length or C-tail deletion mutant (amino acids 263–290) of PD-L1. Site-directed mutagenesis was performed using PCR and verified by sequencing. Vimentin cDNA was amplified from HA-Vim plasmid (46315, Addgene) and cloned into the p3xFlag-CMV-10 vector. The RelA (20012), RelB (20017) and c-Rel (20013) plasmids were purchased from Addgene. Lentiviral shRNAs against CD274, EP300, CREBBP and HDAC2 were purchased from Dharmacon. CD274 cDNA was amplified and subcloned into the pLenti-CMV-Hygro vector. For generating CRISPR cell lines, sgRNAs were subcloned into the pLenti-CRISPRV2 GFP vector (Addgene). The sgRNA sequence for human vimentin KO was 5'-TCCTACCGCAGGATGTTGG-3'; for mouse vimentin, 5'-GTGGCTCCGGCACATCGAGC-3'; for mouse PD-L1, 5'-GTGACCACCAACCCGTGAGT-3'; and for human HDAC2, 5'-CCTCCTTGACTGTACGCCAT-3'.

RT-qPCR analysis. Total RNA was isolated using the Qiagen RNeasy mini kit (Qiagen). cDNA was synthesized using the iScript RT Supermix for RT-qPCR Kit (Bio-Rad), and RT-qPCR was performed using the SYBR Select Master Mix (Thermo Fisher Scientific). Information about the primers is provided in Supplementary Table 9.

Immunoblot and immunoprecipitation. Cells were lysed with EBC buffer (50 mM Tris pH 7.5, 120 mM NaCl, 0.5% NP-40) with protease inhibitors (PIA32953, Thermo Fisher Scientific), phosphatase inhibitors (B15002, Bimake) and/or 2 µM TSA (T8552, Sigma-Aldrich) as described previously⁴⁹. Lysates were separated by SDS-PAGE and transferred to polyvinylidene difluoride membranes. The membranes were incubated with the following antibodies: anti-acetylated Lys (9441, Cell Signaling Technology, CST), anti-human PD-L1 (13684, CST), anti-mouse PD-L1 (EPR20529, ab213480, Abcam), anti-PD-L2 (82723, CST), anti-VISTA (64953, CST), anti-B7-H3 (14058, CST), anti-B7-H4 (14572, CST), anti-galectin-9 (54330, CST), anti-AIF (5318, CST), anti-histone H3 (4499, CST), anti-MEK1/2 (8727, CST), anti-GST (2625, CST), anti-tubulin (T-5168, Sigma-Aldrich), anti-acetylated α-tubulin (Lys40) (5335, CST), anti-c-Jun (9165, CST), anti-vimentin (5741, CST), anti-E-cadherin (3195, CST), anti-KRT17 (4543, CST), anti-KRT19 (sc-376126, Santa Cruz Biotechnology), anti-HIP1R (16814-1-AP, Proteintech Group), anti-HDAC2 (57156, CST), rabbit polyclonal

anti-Myc-tag (2278, CST), mouse monoclonal anti-Myc-tag (2276, CST), anti-HA (MMS-101P, BioLegend), anti-Flag (F-3165, Sigma-Aldrich) or anti-GFP (632381, Clontech). These primary antibodies were used at a dilution of 1:1,000 in 5% non-fat milk. Anti-human PD-L1 extracellular domain (clone 368A.5A4, generated in the laboratory of G.J.F.)⁵⁰ antibodies were used at 1:500 dilution. The anti-acetyl-K263 PD-L1 (acetyl-Lys263-PD-L1) antibodies (generated by ABclonal Technology Biotech) were used at a dilution of 1:200. As secondary antibodies, peroxidase-conjugated anti-mouse secondary antibodies (A-4416, Sigma-Aldrich) or anti-rabbit secondary antibody (A-4914, Sigma-Aldrich) was used at a dilution of 1:3,000. For the detection of Lys 263 acetylation, VeriBlot for IP Detection Reagent (HRP) (ab131366, Abcam) was used at 1:500 dilution. For immunoprecipitation, lysates were incubated with HA-agarose (A-2095, Sigma-Aldrich), Myc-agarose (A-7470, Sigma-Aldrich), Flag-agarose (A-2220, Sigma-Aldrich), anti-PD-L1 clone 29E.12B1 (generated in the laboratory of G.J.F.)⁵¹. Immune complexes were washed five times with NETN buffer (20 mM Tris pH 8.0, 100 mM NaCl, 1 mM EDTA, 0.5% NP-40).

In vivo ubiquitination assays. In vivo ubiquitination assays were performed as described previously^{4,12,43}. Cells were treated with 30 mM MG132 for 6 h before being lysed with buffer A (6 M guanidine-HCl, 0.1 M Na₂HPO₄/NaH₂PO₄ and 10 mM imidazole pH 8.0). Lysates were sonicated and incubated with nickel-nitrilotriacetic acid beads (30230, QIAGEN) for 3 h at room temperature. Subsequently, the beads were washed twice with buffer A, twice with buffer A/TI (1 volume buffer A and 3 volumes buffer TI) and once with buffer TI (25 mM Tris-HCl and 20 mM imidazole (pH 6.8)).

In vitro acetylation assays. Recombinant His-tagged PD-L1 was purified from bacteria. Then, 0.5 µg of His-PD-L1 and/or 0.5 µg of active p300 recombinant protein (81158, Active Motif) were incubated in acetylation assay buffer (50 mM Tris pH 8.0, 0.1 mM EDTA, 50 ng µl⁻¹ BSA) in the presence or absence of 20 µM acetyl-CoA (10101893001, Sigma-Aldrich) for 1 h at 30 °C. For MS analysis, peptide (AA 261–270) was synthesized and purchased from FUJIFILM Wako and 0.5 mg of the peptide was used for the assay.

Immunohistochemistry analysis. Specimens were fixed in 10% formalin-phosphate-buffered solution for 48 h at room temperature and then transferred to 70% ethanol. Subsequently, tissues were paraffin-embedded; 5 µm paraffin sections were used for staining. Sections were deparaffinized, boiled in 10 mM sodium citrate (pH 6.0) for 10 min and incubated with 3% H₂O₂ for 10 min. Blocking and antibody incubations were performed using the Vector M.O.M. Immunodetection kit (BMK-2202; Vector Laboratories). Anti-PD-L1 antibodies were used at 10 µg ml⁻¹ (clone 298B.3C6, generated in the laboratory of G.J.F.)⁵¹. Chromogenic detection was achieved using the Vectastain ABC kit (PK-4000; Vector Laboratories), ImmPACT DAB substrate (SK-4105; Vector Laboratories) and counterstained using Vector Haematoxylin QS (H-3404; Vector Laboratories). Stained sections were finally dehydrated and mounted using Permount.

Immunofluorescence. Cells were fixed in 4% PFA for 15 min, permeabilized with 0.5% Triton X-100 for 15 min and blocked with 10% goat serum for 1 h. To stain frozen tumour tissues samples, 40 µm sections were pretreated with acetone for 10 min. After washing with PBS, cells were stained with rat antibodies against mouse PD-L1 (clone 5C5, generated in the laboratory of G.J.F.)⁵², mouse antibodies against human PD-L1 (clone 9A11, generated in the laboratory of G.J.F.)⁵⁰ or anti-HA-tag antibodies for HA-ins-PD-L1 (2367, Cell Signaling Technology). For HA staining, cells were incubated using the Tyramide Boost Kit (B40941, Thermo Fisher Scientific) according to the manufacturer's protocol (tyramide incubation for 15 min). Cells were then incubated with NucRed Dead nuclear stain (R37113, Thermo Fisher Scientific) for 15 min and washed with PBS. For the mouse PD-L1 and human PD-L1 studies, cells or tissues were stained with donkey anti-rat or donkey anti-mouse secondary antibodies (Alexa Flour 488) for 1 h. Nuclei were stained with DAPI. For Halo-tag imaging⁵³, cells were treated with 0.5 µM HaloTag Alexa Fluor 488 Ligand (G1002, Promega) for 15 min. Images were captured using confocal microscopy (Nikon Ti inverted or Zeiss LSM880) and assembled using Fiji software.

Cell fractionation assays. Cells were collected using EDTA and then counted to adjust cell numbers for each sample. Fractionation was performed using the Cell Fractionation kit (9038, Cell Signaling Technology) or the Subcellular Protein Fractionation kit (78840, Thermo Fisher Scientific). The pellet was washed once using cold PBS between every step.

DNA binding assays. To prepare biotin-DNA, two oligos (5'-bio-TGCAGCTGGCACGACAGGTTGCAGCGAGTC-3'; and 5'-GAATCGCTGCAACCTGTCGTGCCAGCTGCA-3') were annealed. To prepare DNA-conjugated beads, 200 µl of 0.5 µM biotin-DNA was incubated with streptavidin-coated agarose beads (20349, Thermo Fisher Scientific) in DNA binding buffer (10 mM Tris-HCl pH 7.5, 100 mM NaCl, 10% glycerol, 0.01% NP-40 and 10 µg ml⁻¹ BSA) at room temperature for 1 h, and then washed with DNA binding buffer. The beads were incubated with 1,000 µg of lysate in the DNA

binding buffer at 4°C for 2 h and washed with binding buffer before analysis using immunoblotting.

ChIP and ChIP-seq. ChIP was performed with anti-HA-tag antibodies (Abcam, ab9110) in MDA-MB-231 CD274-KO cells stably expressing HA-tagged PD-L1. For replicate 1, ChIP was performed using the Diagenode iDeal ChIP-seq Kit for Transcription Factors (Diagenode, C01010055) with the addition of ChIP cross-link Gold cross-linking reagent (C01019027). Library preparation and sequencing analysis were performed at the Molecular Biology Core facility in Dana-Farber Cancer Institute. For replicate 2, ChIP was performed as described previously⁵⁴. Qualified libraries were deep-sequenced using an Illumina HiSeq 4000 system according to the manufacturer's instructions at the Northwestern University.

ChIP-seq data analyses. ChIP-seq reads were aligned to the non-random chromosomes of the human (hg38 assembly) genome using Bowtie 2 v.2.2.9 (ref. ⁵⁵, using the default parameters). Peak calling was performed using MACS2 v.2.1.1 (ref. ⁵⁶) with corresponding input controls (using the default parameters, except for the following: --broad and --broad-cutoff 0.05). Bedtools v.2.27.1 was used to acquire common PD-L1-binding peaks from two replicates. The GREAT software v.4.0.4 (ref. ⁵⁷; using the default parameters) was used to assign peaks to genes of the human hg38 assembly, and PAVIS⁵⁸ (using the default parameters) was used for the peak gene annotation. De novo motif analysis was performed using HOMER v.4.10.3 among the list of sites with significant PD-L1 binding in both replicates. Selected enriched regions were aligned with each other according to the position of TSS. For each experiment, the ChIP-seq density profiles were normalized to the density per million total reads. Metagene plots and heat maps were generated using ngsplot v.2.61 with colour saturation as indicated. For the colocalization study, the publicly available MDA-MB-231 ChIP-seq datasets were downloaded from the GEO database. These datasets were aligned to the hg38 genome using the Bowtie 2 v.2.2.9 (ref. ⁵⁵) with the same parameters as for the PD-L1 ChIP-seq datasets. BigWig file generation for each dataset and colocalization calculation were performed using deepTools v.2.5.3 (ref. ⁵⁹).

MS analysis. To identify the binding proteins of PD-L1, HEK293T cells were transfected with pcDNA3-Flag vector, Flag-tagged PD-L1, pcDNA3-HA vector or HA-ins-PD-L1. Lysates were immunoprecipitated with Flag-agarose or HA-agarose, and then binding proteins were eluted with 2% SDS. Immunoprecipitates were digested with trypsin (V5111, Promega) overnight. The peptides were resolved with 0.1% formic acid, desalted using C18 StageTips (Thermo Fisher Scientific) and redissolved in 0.1% formic acid. The obtained peptides were assayed using a nanoLC-Ultra 2D coupled with a TripleTOF 5600 mass spectrometer (AB SCIEX) and analysed using 2D-ICAL, v.1.3.23. GO enrichment analysis was performed using Metascape⁶⁰. To detect Lys 263 acetylation of PD-L1, following the in vitro acetylation assay, the synthetic peptides were measured using a QTRAP5500 mass spectrometer and analysed using ProteinPilot v.3.0.

RNA-seq and bioinformatics analyses. Total RNA from MDA-MB-231 WT, MDA-MB-231 CD274-KO, CT26 WT or CT26 Cd274-KO cells was purified using the Qiagen RNeasy mini kit (Qiagen). Library preparation (Kapa mRNASeq Hyper prep, Roche) and sequencing analysis (Illumina NS500 Single-End 75 bp) were performed at the Molecular Biology Core facility at the Dana-Farber Cancer Institute. Total RNAs from CT26 Cd274-KO cells re-expressing WT or Cd274^{K26Q} were purified using the Qiagen RNeasy mini kit (Qiagen). Library preparation and sequencing analysis (BGISEQ-500, Single-End 50 bp) were performed by BGI Hong Kong RNA-seq; data were aligned to mm10 and hg38 using STAR v.2.5.4a⁶¹ (using the default parameters, except the following: --outSAMstrandField intronMotif, --outFilterIntronMotifs RemoveNoncanonical). Differential gene expression analysis was performed using Cufflinks v.2.2.1 (ref. ⁶²). A significant change was defined as a *q* value (adjusted *P* value using the Benjamini–Hochberg procedure) of <0.05. Prediction of transcription factors regulating differentially expressed genes was analysed by MetaCore software v.6.33. GO analysis for enriched 'biological process' terms was performed using the web tool DAVID Bioinformatics Database v.6.8 (<https://david.ncifcrf.gov/tools.jsp>)^{63,64} for the 'GOTERM_BP_DIRECT' category. For GSEA analysis, we used the GSEA tool v.3.0, with the MSigDB v.6.2 Hallmarks gene sets collection and the 'classic' method for calculating enrichment scores⁶⁵.

Transcripts and survival analyses. HDAC2 or vimentin transcripts across all cancer types and the overall survival studies of common cancer types were analysed using the gene expression profiling interactive analysis GEPIA (<http://gepia.cancer-pku.cn>)⁶⁶. The customized genomic analysis was based on The Cancer Genome Atlas (TCGA) data. The expression data of CD274, PDCD1LG2 and VSIR in a panel of breast cancer cell lines (*n*=56) were obtained from GEO dataset GSE36139. The data for vimentin expression and survival of patients with melanoma after PD-1 antibody treatment were generated using the TIDE tool (<http://tide.dfci.harvard.edu>)⁶⁷ and the source data are based on the Riaz2017_PD1 cohort⁶⁸.

In vivo experimental therapy in mouse models. The study is compliant with all relevant ethical regulations regarding animal research. Animal experiments

were approved by Dana-Farber Cancer Institute Institutional Animal Care and Use Committee (protocol, 04-047) or the Beth Israel Deaconess Medical Center (BIDMC) Institutional Animal Care and Use Committee (protocol, 043-2015), and were performed in accordance with guidelines established by the NIH Guide for the care and use of laboratory animals. The syngeneic MC38 and MC38 Cd274^{K26Q} cancer models were established by subcutaneously injecting 1×10^5 of MC38 cells in 100 µl HBSS saline buffer into the right flank of female C57BL/6 mice (aged 6–8 weeks; Jackson Laboratory). For the MC38 nude mice model, cells were injected into the right flank of female nude mice (aged 6–8 weeks; T-cell deficient, Taconic NCRNU-F). For the CT26 model, 5×10^4 of the indicated CT26 subclone cells were injected into the right flanks of BALB/c female mice (aged 6–8 weeks; Jackson Laboratory). For the B16F10 primary and metastasis model, primary tumours were generated by subcutaneous injection of 2×10^4 B16F10 cells into female C57BL/6 mice (aged 6–8 weeks; Jackson Laboratory). Tumours were dissected and measured after 4 weeks. Lung metastases were generated by tail vein injection of 2.5×10^4 B16F10 cells into female C57BL/6 mice (aged 6–8 weeks) and collecting the lungs for metastasis analysis at 4 weeks. Tumour sizes were measured every 3 d after implantation and tumour volume was calculated as follows: length \times width $^2 \times 0.5$. On day 7 after injection, mice were pooled and randomly divided. For the MC38 model, mice were grouped into four groups as follows: control antibodies, PD-1 monoclonal antibodies (clone 29F.1A12), HDAC2 inhibitor santacruzamate A and PD-1 monoclonal antibodies + santacruzamate A. For the CT26 model, the mice were split into two groups (control antibodies and PD-1 monoclonal antibodies). The control and PD-1 monoclonal antibody treatments were conducted by intraperitoneal injection (200 µg per mouse in 200 µl HBSS saline buffer) every 3 d for a total of eight injections. Santacruzamate A treatment was given by intraperitoneal injection once a day with a dosage of 25 mg kg^{-1} (in 5% DMSO, 5% PEG 300, 5% Tween-80 in double-distilled H₂O) for three weeks with a break every week for 1 d. For the survival studies, animals were monitored for tumour volumes for 60 d, until the tumour volume exceeded 1,000 mm 3 , or until the tumour became ulcerated with the ulcer diameter reaching 1 cm. Statistical analysis was conducted using GraphPad Prism. Kaplan–Meier curves and the corresponding Gehan–Breslow–Wilcoxon tests were used to evaluate statistical differences between groups in the survival studies.

TIL analysis. Nine days after the treatment of MC38 tumours with the indicated compounds, TILs were isolated and stained. For stimulation, cells were incubated with a cell-stimulation cocktail (PMA and Ionomycin) plus protein-transport inhibitor (brefeldin A and menesin) for 4 h. Cells were analysed using multicolour flow cytometry (BD LSR Fortessa X-20). The following antibodies were used: anti-CD45 BV605 (103140, Biolegend); anti-CD3 BV875 (100355, Biolegend); anti-CD4 BV650 (100469, Biolegend); anti-CD8 (100784, Biolegend); anti-FOXP3 PerCP-Cy5.5 (563902, BD); anti-TNF α APC (506308, Biolegend); anti-IFN γ FITC (505806, Biolegend); anti-IL-2 BV510 (503833, Biolegend); anti-IL-10 PerCP-Cy5.5 (505028, Biolegend). All analyses were performed using FlowJo v.10.6.1 (Tree Star). The gating strategy was as follows: first, gate cells excluding dead cells and debris on the basis of cell size; then gate live cells on the basis of live–dead NIR negative cells; then gate CD45 $^+$ cells; then gate CD45 $^+$ CD3 $^+$ cells; and then gate CD45 $^+$ CD3 $^+$ CD8 $^+$ cells and CD45 $^+$ CD3 $^+$ CD4 $^+$ cells. Cytokine expression was determined in the populations of CD45 $^+$ CD3 $^+$ cells.

Statistics and reproducibility. All quantitative data are presented as mean \pm s.e.m. or mean \pm s.d., as indicated, of at least three independent experiments or biological replicates. Statistical analyses were performed using GraphPad Prism 7 and Excel 2016 unless indicated otherwise. *P* values were calculated as described in the figure legend for each experiment. All statistical tests were performed two-sided. *P* < 0.05 was considered to be statistically significant. All data shown are representative of two or more independent experiments with similar results, unless indicated otherwise.

Reporting Summary. Further information on research design is available in the Nature Research Reporting Summary linked to this article.

Data availability

The next-generation sequencing data generated in this study have been submitted to the Gene Expression Omnibus Database under the accession numbers GSE134510, GSE146557 and GSE146648. The data from MS analysis was deposited at the Japan Proteome Standard Repository/Database (JPOST) under the accession numbers JPST000666/PXD015191 and JPST000757/PXD017707, respectively. The human cancer data were derived from the TCGA Research Network (<http://cancergenome.nih.gov/>) and the Riaz2017_PD1 cohort⁶⁸. The dataset derived from this resource that supports the findings of this study is available at GEPIA (<http://gepia.cancer-pku.cn>)⁶⁶ and TIDE (<http://tide.dfci.harvard.edu>)⁶⁷. All other data supporting the findings of this study are available from the corresponding authors on reasonable request. Source data are provided with this paper.

Code availability

Custom scripts used in the study are available at https://github.com/ejgkelvin/Nuclear_PD-L1_Acetylation.

References

47. Nelson-Rees, W. A., Daniels, D. W. & Flandermeyer, R. R. Cross-contamination of cells in culture. *Science* **212**, 446–452 (1981).
48. Dai, X. et al. Prostate cancer-associated SPOP mutations confer resistance to BET inhibitors through stabilization of BRD4. *Nat. Med.* **23**, 1063–1071 (2017).
49. Wei, W. et al. Degradation of the SCF component Skp2 in cell-cycle phase G1 by the anaphase-promoting complex. *Nature* **428**, 194–198 (2004).
50. Mahoney, K. M. et al. PD-L1 antibodies to its cytoplasmic domain most clearly delineate cell membranes in immunohistochemical staining of tumor cells. *Cancer Immunol. Res.* **3**, 1308–1315 (2015).
51. Chaudhri, A. et al. PD-L1 binds to B7-1 only in *cis* on the same cell surface. *Cancer Immunol. Res.* **6**, 921–929 (2018).
52. Liang, S. C. et al. Regulation of PD-1, PD-L1, and PD-L2 expression during normal and autoimmune responses. *Eur. J. Immunol.* **33**, 2706–2716 (2003).
53. Svendsen, S., Zimprich, C., McDougall, M. G., Klauert, D. H. & Los, G. V. Spatial separation and bidirectional trafficking of proteins using a multi-functional reporter. *BMC Cell Biol.* **9**, 17 (2008).
54. Zeng, H. et al. Systematic identification of Ctr9 regulome in ERα-positive breast cancer. *BMC Genom.* **17**, 902 (2016).
55. Langmead, B. & Salzberg, S. L. Fast gapped-read alignment with Bowtie 2. *Nat. Methods* **9**, 357–359 (2012).
56. Zhang, Y. et al. Model-based analysis of ChIP-Seq (MACS). *Genome Biol.* **9**, R137 (2008).
57. McLean, C. Y. et al. GREAT improves functional interpretation of *cis*-regulatory regions. *Nat. Biotechnol.* **28**, 495–501 (2010).
58. Huang, W., Loganathanraj, R., Schroeder, B., Fargo, D. & Li, L. PAVIS: a tool for peak annotation and visualization. *Bioinformatics* **29**, 3097–3099 (2013).
59. Ramirez, F., Dundar, F., Diehl, S., Gruning, B. A. & Manke, T. DeepTools: a flexible platform for exploring deep-sequencing data. *Nucleic Acids Res.* **42**, W187–W191 (2014).
60. Zhou, Y. et al. Metascape provides a biologist-oriented resource for the analysis of systems-level datasets. *Nat. Commun.* **10**, 1523 (2019).
61. Dobin, A. et al. STAR: ultrafast universal RNA-seq aligner. *Bioinformatics* **29**, 15–21 (2013).
62. Trapnell, C. et al. Differential gene and transcript expression analysis of RNA-seq experiments with TopHat and Cufflinks. *Nat. Protoc.* **7**, 562–578 (2012).
63. Huang da, W., Sherman, B. T. & Lempicki, R. A. Systematic and integrative analysis of large gene lists using DAVID bioinformatics resources. *Nat. Protoc.* **4**, 44–57 (2009).
64. Huang da, W., Sherman, B. T. & Lempicki, R. A. Bioinformatics enrichment tools: paths toward the comprehensive functional analysis of large gene lists. *Nucleic Acids Res.* **37**, 1–13 (2009).
65. Subramanian, A. et al. Gene set enrichment analysis: a knowledge-based approach for interpreting genome-wide expression profiles. *Proc. Natl Acad. Sci. USA* **102**, 15545–15550 (2005).
66. Tang, Z. et al. GEPIA: a web server for cancer and normal gene expression profiling and interactive analyses. *Nucleic Acids Res.* **45**, W98–W102 (2017).
67. Jiang, P. et al. Signatures of T cell dysfunction and exclusion predict cancer immunotherapy response. *Nat. Med.* **24**, 1550–1558 (2018).
68. Riaz, N. et al. Tumor and microenvironment evolution during immunotherapy with nivolumab. *Cell* **171**, 934–949 (2017).

Acknowledgements

We thank J. Guo, F. Dang and other members of the Wei laboratory for reading the manuscript, as well as members of the Wei, Freeman and Sicinski laboratories for helpful discussions. We thank staff at the Microscopy Resources on the North Quad (MicRoN) core at Harvard Medical School for helping with IF experiments. This research was supported in part by the NIH grants (R01CA177910 and R01GM094777, to W.W.; P50CA101942, to G.J.F.; R01CA236226 and R01CA202634, to P.S.; and R01CA236356, to W.X.); the Japan Society for Promotion of Science (JSPS) KAKENHI Grant (JP18H06157, to N.T.N.). N.T.N. is supported by JSPS Research Fellowships for Young Scientists and the Osamu Hayashi Memorial Scholarship for Study Abroad.

Author contributions

Y.Gao, N.T.N. and X.B. designed and performed the experiments with assistance from J.Z., C.C., Y.F., Y.-H.H., L.M. A.K., X.D., S.S., Y.Geng, D.W., H.I., B.J.N. and L.L.; N.T.N., M.O., A.N. and J.L. performed the MS analysis. A.K., W.X. and N.T.C. performed the ChIP experiments. H.L., A.N. and M.O. analysed the data. C.C. and X.S.L. helped with the bioinformatics analysis. Y.M., P.S., G.J.F. and W.W. guided and supervised the study. N.T.N., Y.Gao, J.Z. and W.W. wrote the manuscript. All of the authors commented on the manuscript.

Competing interests

G.J.F. is an inventor on patents covering the PD-1/PD-L1 pathway including US Patent Nos. 6,808,710; 7,038,013; 7,101,550; 7,105,328; 7,638,492; 7,700,301; 7,432,059; 7,709,214; and 7,722,868 and associated foreign patent issuances. These patents have been licensed non-exclusively to Roche, Merck, Bristol-Myers-Squibb, EMD-Serono, Boehringer-Ingelheim, AstraZeneca, Leica, Mayo Clinic, Dako and Novartis and several research reagent providers; and he receives royalties based on those licenses. G.J.F. was recently determined to be an inventor on US Patent Nos. 7,595,048; 8,168,179; 8,728,474; 9,067,999; 9,073,994; and 9,402,899 covering the PD-1/PD-L1 pathway and may in the future receive royalty payments based on licenses to those patents. G.J.F. has served on the advisory boards for Roche, Bristol-Myers-Squibb, Xios, Origimed, Triurus, iTeos, NextPoint, IgM and Jubilant. G.J.F. has equity in Nextpoint, Triurus, Xios, iTeos, IgM, and GV20.

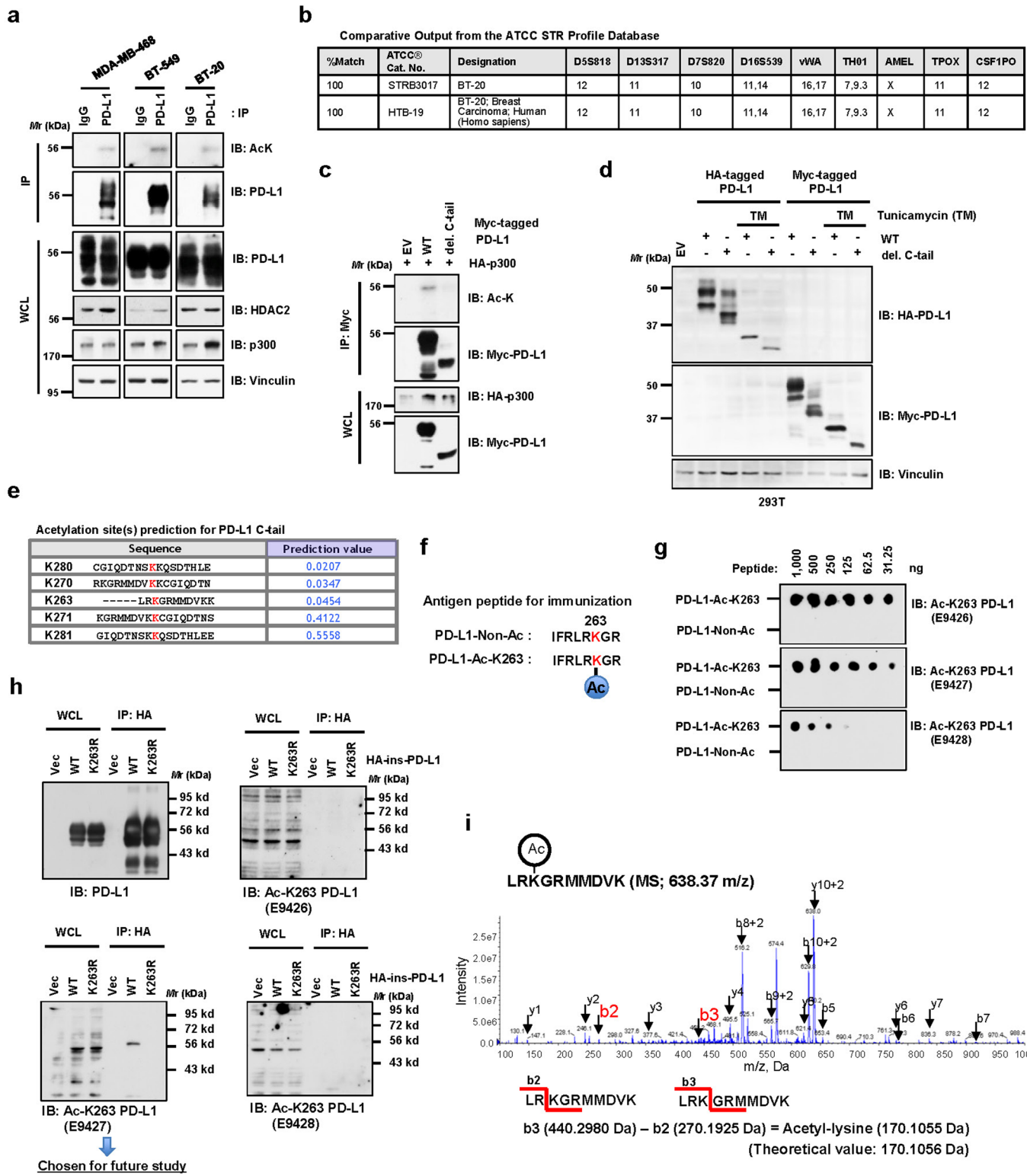
Additional information

Extended data is available for this paper at <https://doi.org/10.1038/s41556-020-0562-4>.

Supplementary information is available for this paper at <https://doi.org/10.1038/s41556-020-0562-4>.

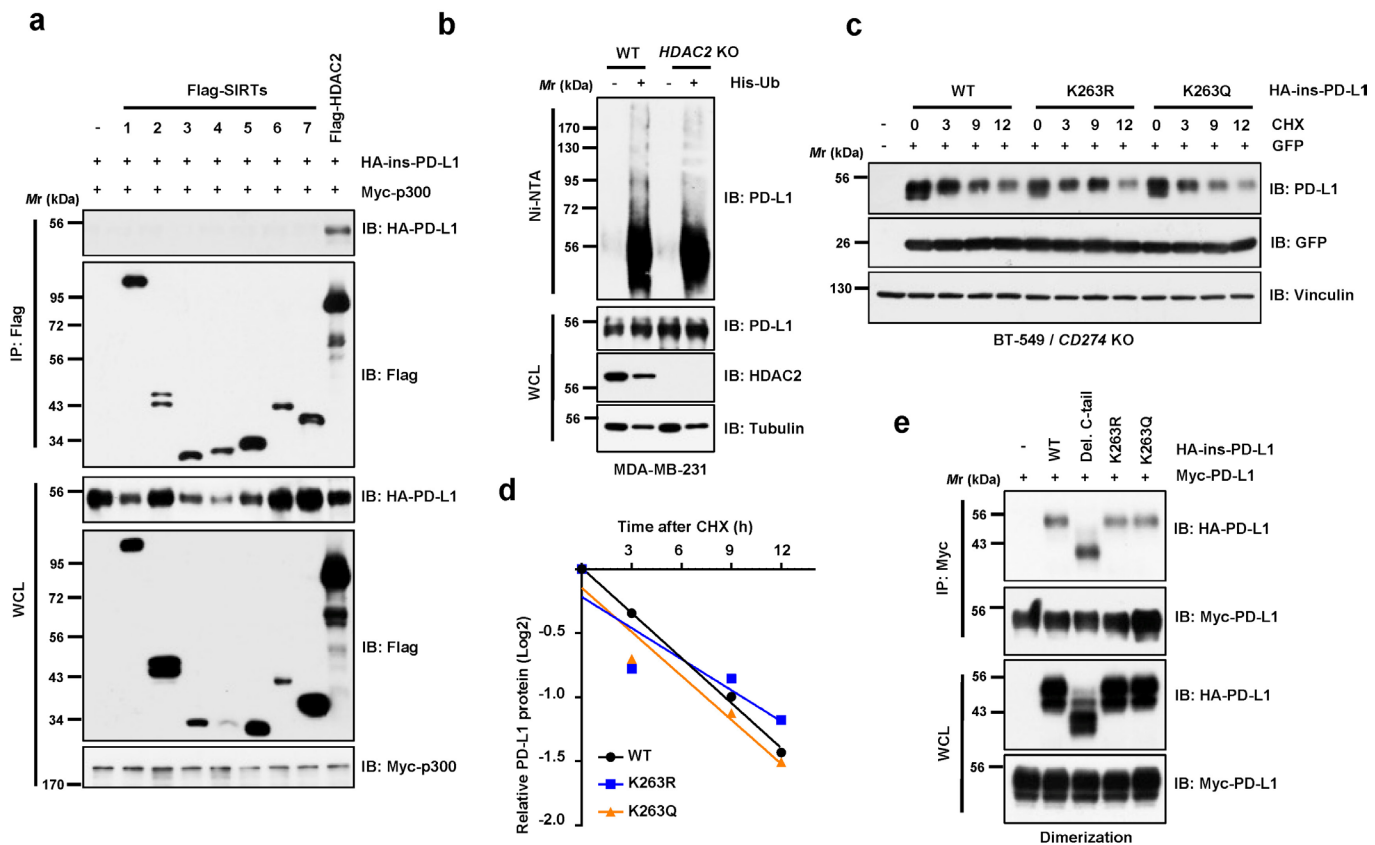
Correspondence and requests for materials should be addressed to Y.M., P.S., G.J.F. or W.W.

Reprints and permissions information is available at www.nature.com/reprints.

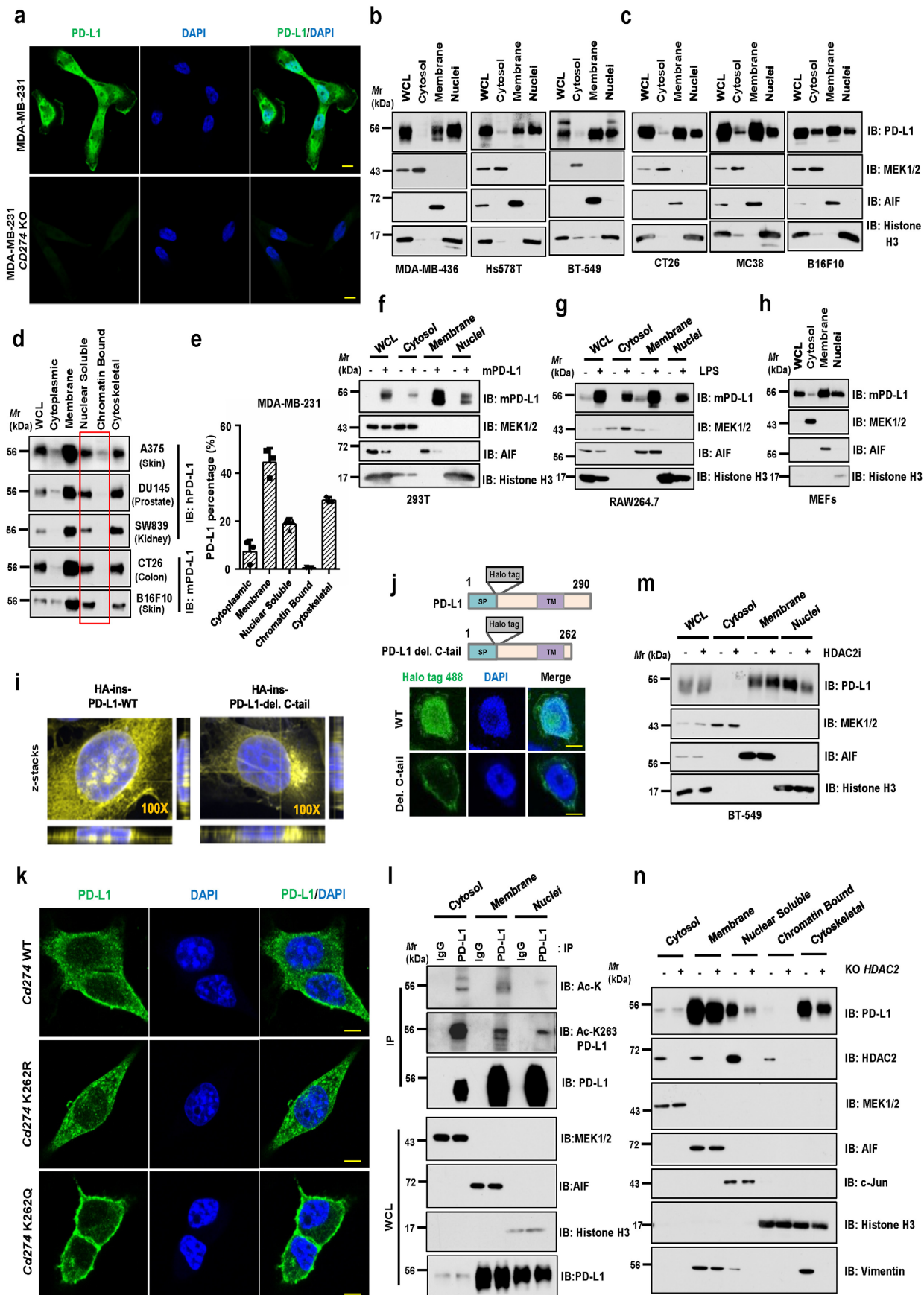


Extended Data Fig. 1 | See next page for caption.

Extended Data Fig. 1 | Lysine 263 (K263) within the cytoplasmic domain of PD-L1 is acetylated. **a**, Immunoblot (IB) analysis of whole-cell lysates (WCL) and anti-PD-L1 immunoprecipitates (IPs) derived from MDA-MB-468, BT-549 and BT-20 cells. Immunoglobulin G (IgG) served as a negative control. **b**, Authentication results of the BT-20 cell line performed by ATCC. **c**, IB analysis of WCL and anti-Myc IPs derived from 293T cells transfected with HA-p300 and Myc-wild type (WT) PD-L1 or the deletion mutant of C-tail (amino acids (AA) 263-290). **d**, IB analysis of WCL derived from 293T cells transfected with HA-tag-inserted (HA-ins) or Myc-tagged wild-type (WT) or del. C-tail PD-L1 with or without 1 µg/ml tunicamycin treatment overnight. **e**, Predicted lysine acetylation sites by the Web Server for KAT-specific Acetylation Site Prediction (ASEB) analysis. **f**, A schematic diagram of the PD-L1 Lys263 acetylated peptide and non-acetylated peptide used for immunization to generate the anti-Ac-K263 PD-L1 antibody. **g**, Dot-blot testing of acetylated and non-acetylated peptides using indicated purified antibodies. **h**, IB analysis of WCL and anti-HA IPs derived from 293T cells transfected with HA-ins-PD-L1 WT or the K263R mutant. **i**, Mass-spectrometry detection of Lys263 acetylation using a synthetic peptide (AA 261 to 270) following *in vitro* acetylation assay. The blots and western blots in **a**, **c**, **d**, **g** and **h** were performed for n=2 independent experiments with similar results. Unprocessed immunoblots are shown in Source Data Extended Data Fig. 1.

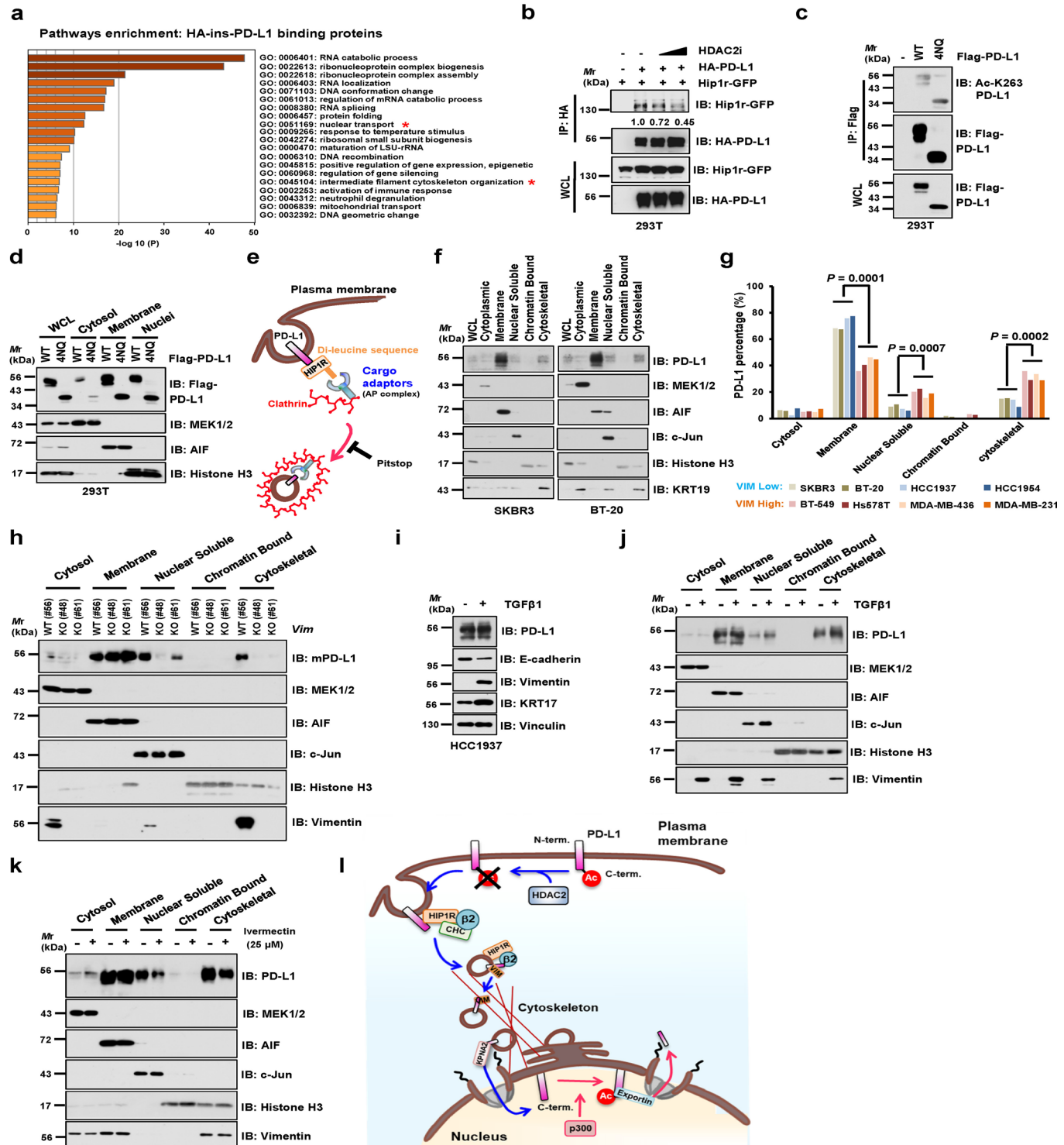


Extended Data Fig. 2 | HDAC2 mediates deacetylation of PD-L1. **a**, IB analysis of WCL and anti-Flag IPs derived from 293T cells transfected with Myc-p300, HA-ins-PD-L1 and/or Flag-tagged deacetylases. **b**, IB analysis of WCL and Ni-NTA pull-down products from MDA-MB-231 WT and HDAC2 knockout (KO) cells transfected with His-Ub and treated with 10 μ M MG-132 overnight. **c**, **d**, IB analysis of WCL derived from BT-549 CD274 KO cells transfected with HA-PD-L1 WT, K263R or K263Q mutants and treated with 150 μ g/ml cycloheximide (CHX) for indicated hours (**c**). Signal intensity of PD-L1 protein was quantified by ImageJ as indicated (**d**). **e**, IB analysis of WCL and anti-Myc IPs derived from 293T cells transfected with indicated constructs. Western blots in **a-c** and **e** were performed for n=2 independent experiments with similar results. Unprocessed immunoblots are shown in Source Data Extended Data Fig. 2.

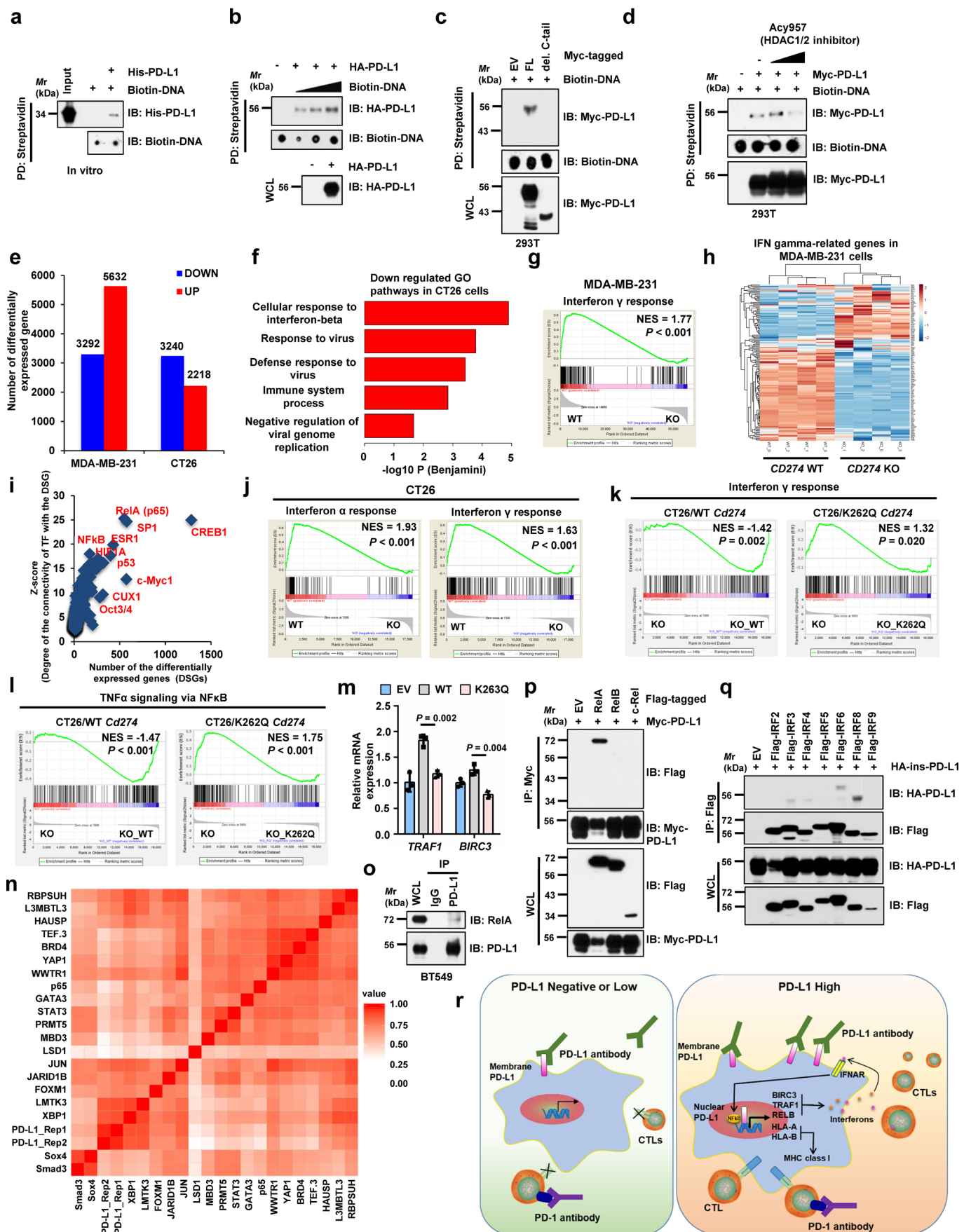


Extended Data Fig. 3 | See next page for caption.

Extended Data Fig. 3 | Lysine 263 (K263) acetylation regulates PD-L1 nuclear translocation. **a**, Immunofluorescence (IF) staining of human PD-L1 (clone 9A11) and DAPI of MDA-MB-231 WT and CD274 KO cells. Scale bars, 10 μ m. **b, c**, Fractionation analysis using kit from Cell Signaling Technology (CST, #9038) for PD-L1 in human MDA-MB-436, Hs578T and BT-549 cells (**b**), as well as in mouse CT26, MC38, and B16F10 cells (**c**). **d**, Fractionation analysis using kits from Thermo Fisher Scientific™ (#78840) for PD-L1 in indicated cell lines. **e**, Quantification of PD-L1 protein abundance of indicated compartments in MDA-MB-231 cells. Data were presented as mean \pm s.d. (n=3 biologically independent samples). **f**, Fractionation analysis for PD-L1 from 293T cells transfected with mouse PD-L1. **g, h**, Fractionation analysis for PD-L1 in RAW264.7 cells stimulated with 1 μ g/ml Lipopolysaccharide (LPS) for 16 hours (**g**) and in mouse embryonic fibroblasts (**h**). **i**, Z-stacks confocal microscopy images (3x close-up of the source picture) for IF study in Fig. 3d. PD-L1, yellow color and DAPI, blue. **j**, Fluorescence images of MDA-MB-231 CD274 KO cells transduced with Halo-PD-L1 (AF488) or its C-tail deletion mutant. Scale bars, 5 μ m. **k**, IF staining of mouse PD-L1 (clone 5C5) in CT26 Cd274 KO cells transduced with mouse Cd274 WT, K262R or K262Q mutant lentivirus. Scale bars, 5 μ m. **l**, IB analysis of WCL and anti-PD-L1 IPs derived from indicated fractions of MDA-MB-231 cells. **m**, Fractionation analysis for BT-549 cells treated with 50 μ M HDAC2 inhibitor for 6 hrs. **n**, Fractionation analysis for PD-L1 in MDA-MB-231 WT or HDAC2 KO cells. The Western blots in **b-d, f-h, l-n**, and IF studies in **a, j** and **k** were performed for n=2 independent experiments with similar results. Unprocessed immunoblots are shown in Source Data Extended Data Fig. 3.

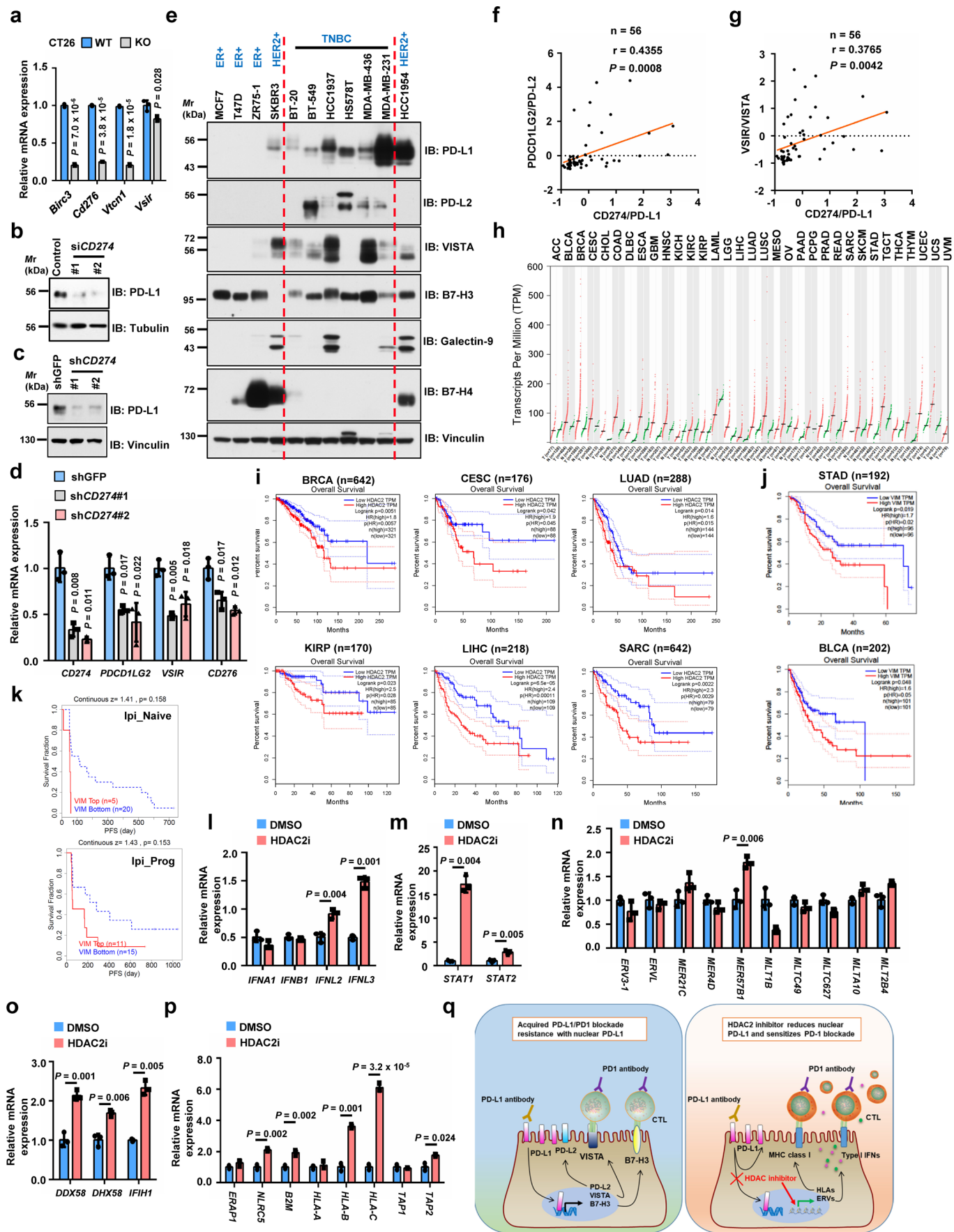


Extended Data Fig. 4 | Protein interacting network likely mediates PD-L1 nuclear-translocation process. **a**, Results from mass spectrometry analysis were analyzed for GO term enrichment. Red stars denote pathways associated with protein translocation. n = 2 independent experiments with similar results. P values were calculated using hypergeometric test. **b**, IB of WCL and anti-HA IPs derived from 293T cells transfected with HA-ins-PD-L1 and mouse Hip1r-GFP, and treated with HDAC2 inhibitor for 6 hrs. **c**, IB of WCL and anti-Flag IPs derived from 293T cells transfected with PD-L1 WT or glycosylation-deficient 4NQ (N35, N192, N200 and N219) mutant. **d**, Fractionation analysis for PD-L1 from 293T cells transfected with WT or the glycosylation-deficient 4NQ mutant. **e**, Schematic diagram depicting the working model for endocytosis of PD-L1 from plasma membrane. **f**, Fractionation analysis for PD-L1 in Vimentin-low SKBR3 and BT-20 cells. **g**, Relative abundance of PD-L1 protein in each fraction was quantified and calculated for percentage. Statistics, two-tailed Student's t-test. **h**, Fractionation analysis for PD-L1 in CT26 WT and Vim KO clones. **i**, IB of HCC1937 cells treated with 10 ng/ml Transforming Growth Factor-β1 (TGFβ1) for 14 days. **j**, Fractionation analysis for PD-L1 in HCC1937 cells treated with 10 ng/ml TGFβ1 for 14 days. **k**, Fractionation analysis for PD-L1 in MDA-MB-231 cells treated with vehicle or 25 μM Ivermectin (IVM) for 2 hrs. **l**, A schematic diagram to show the working model for nuclear translocation of PD-L1 from plasma membrane. Western blots in **b-d**, **f**, and **h-k** were performed for n=2 independent experiments with similar results. Unprocessed immunoblots are shown in Source Data Extended Data Fig. 4. Statistical source data are available in Statistical Source Data Extended Data Fig. 4.



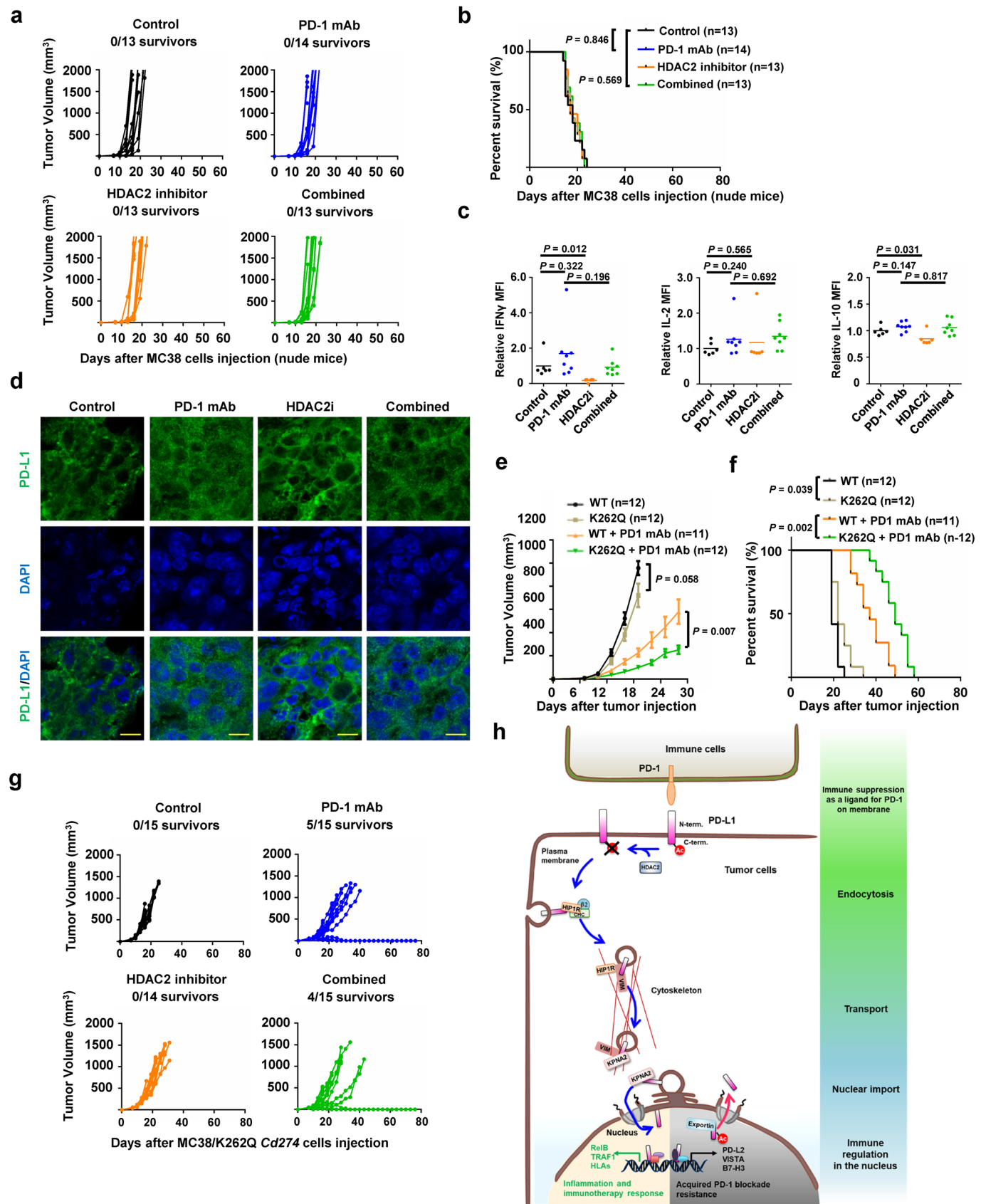
Extended Data Fig. 5 | See next page for caption.

Extended Data Fig. 5 | Nuclear PD-L1 likely stimulates the gene expression of pro-inflammation pathways. **a**, DNA binding assays of purified PD-L1 with biotinylated DNA *in vitro*. **b, c**, DNA binding assays of biotinylated DNA and 293T cells transfected with indicated constructs. **d**, DNA binding assays of transfected 293T cells treated with Acy957. **e**, Numbers of differentially expressed genes upon *CD274* or *Cd274* KO. **f**, Top 5 enriched immune response-related GO terms upon *Cd274* KO in CT26 cells, analyzed by Fisher-exact test with Benjamini-Hochberg correction. **g**, GSEA signature upon *CD274* KO in MDA-MB-231 cells. **h**, Heatmap display of interferon γ genes upon *CD274* KO in MDA-MB-231 cells. **i**, Prediction analysis for transcription factors regulating down-regulated genes upon *CD274* KO in MDA-MB-231 cells. **j**, GSEA signatures upon *Cd274* KO in CT26 cells. **k, l**, GSEA signatures of pathways in CT26 *Cd274* KO cells restored WT or K262Q mutant *Cd274*. **m**, RT-qPCR analysis of BT-549 *CD274* KO cells transfected with *CD274* WT or K263Q mutants. Data are shown as mean \pm s.d. of n=3 independent experiments. Statistics, two-tailed Student's t-test. **n**, Hierarchical clustering of ChIP-seq binding profiles and two replicates of PD-L1 binding profiles genome-wide in MDA-MB-231 cells. **o**, IB of WCL and anti-PD-L1 IPs derived from MDA-MB-231 cells. **p, q**, IB of WCL and IPs derived from 293T cells transfected with indicated constructs. **r**, Schematic diagram showing how nuclear PD-L1 enhances the immunotherapy response through affecting expression of immune-related genes. GSEA analyses in **g** and **j-l** were performed using Kolmogorov-Smirnov statistic. Biologically independent sequenced samples/group for **f-j**, n=4; for **k** and **l**, n=3. The blots and Western blots in **a-d** and **o-q** were performed for n=2 independent experiments with similar results. Unprocessed immunoblots are shown in Source Data Extended Data Fig. 5. Statistical source data are available in Statistical Source Data Extended Data Fig. 5.



Extended Data Fig. 6 | See next page for caption.

Extended Data Fig. 6 | PD-L1 expression levels correlate with and regulate immune-checkpoint genes. **a**, RT-qPCR analysis of genes upon Cd274 KO in CT26 cells. **b**, IB of MDA-MB-231 cells transfected with control or CD274 siRNAs. **c, d**, IB (**c**) and RT-qPCR (**d**) analysis of MDA-MB-231 cells with CD274 knockdown by shRNAs. **e**, IB of WCL derived from breast cancer cell lines. **f, g**, Pearson correlation (two-tailed) analysis for PD-L1 mRNA (Z-score) with PD-L2 (**f**) or VISTA (**g**) in breast cancer cell lines (GSE36139). Red line, linear regression line. **h**, HDAC2 expression profiled by GEPIA. Tumour (T), red dots; normal tissues (N), green dots. **i**, Overall survival of patients with high (>70%, red curve) and low (<30%, blue curve) HDAC2 (**i**) or Vimentin (**j**) analyzed using Log-rank test by GEPIA. **k**, Progression-free survival (PFS) of melanoma patients (Riaz2017_PD1 cohort, PMID:29033130) treated with PD-1 mAb (Nivolumab) with high or low VIM expression analyzed using Kaplan-Meier curves by TIDE. Ipi_Naive, ipilimumab-naïve (n=25); Ipi_Prog, progressed on ipilimumab (n=26). **l-p**, RT-qPCR of MDA-MB-231 cells treated with vehicle or HDAC2 inhibitor. These genes are involved in Type I or III interferon pathways (**l**), STAT1/2 pathways (**m**), endogenous retrovirus ERVs (**n**), double-stranded pattern recognition receptors (**o**), antigen presenting and presentation via MHC class I (**p**). **q**, Schematic diagram to show a possible molecular mechanism of acquired PD-1/PD-L1 blockade resistance caused by nuclear PD-L1 (left), and the potential usage of HDAC2 inhibitor (right). Tumor abbreviations are shown in GEPIA. Western blots **b-c** and **e** were performed for n=2 independent experiments with similar results. PCR data **a, d** and **l-p** were shown as mean \pm s.d. of n=3 independent experiments, analyzed by two-tailed Student's t-test. Unprocessed immunoblots are shown in Source Data Extended Data Fig. 6. Statistical source data are available in Statistical Source Data Extended Data Fig. 6.



Extended Data Fig. 7 | See next page for caption.

Extended Data Fig. 7 | Targeting HDAC2 and inhibiting PD-L1 deacetylation can enhance immunotherapy efficacy. **a, b**, Tumour growth (**a**) and survival curves (**b**) of nude mice bearing MC 38 tumors treated with control antibody, PD-1 mAb, HDAC2 inhibitor or combined therapy. **c**, TILs from treated MC38 syngeneic tumours (Control, n=6; PD-1 mAb, n=8; HDAC2i, n=6; Combined, n=8) after stimulation were analyzed for Interferon γ (IFN γ), IL-2 and IL-10. **d**, Immunofluorescence for PD-L1 and DAPI of MC38 syngeneic tumours treated as indicated. Scale bars, 10 μ m. n=4 independent samples per group. **e, f**, Tumour growth (**e**) and survival curves (**f**) of BALB/c mice bearing tumor derived from CT26-Cd274 KO cells with re-introduced WT or K262Q Cd274, treated with control antibody or PD-1 mAb. Tumour volume was shown as mean \pm s.d. Statistics in **e**, two-tailed Student's t-test. **g**, Tumour growth of MC38/K262Q Cd274 tumour-bearing C57BL/6 mice treated as indicated. **h**, A schematic diagram of molecular mechanism underling nuclear translocation of PD-L1 and its contradictory functions in immune response. PD-L1 deacetylated by HDAC2 is translocated into the nucleus via interacting with various key regulatory proteins for endocytosis and nuclear translocation, then transactivates immune responsive in the nucleus to impact tumour sensitivity to PD-1 blockage (the lower left panel with yellow background), as well as controlling various immune checkpoint gene expression to possibly confer resistance to PD-1 blockage treatment (the lower right panel with gray background). Thus, HDAC2 inhibitor will reduce PD-L1 nuclear localization to prevent the emerging resistance to PD-1 blockade treatment. P values in **b** and **f** were calculated using Gehan-Breslow-Wilcoxon test, two-sided. Statistical source data are available in Statistical Source Data Extended Data Fig. 7.

Reporting Summary

Nature Research wishes to improve the reproducibility of the work that we publish. This form provides structure for consistency and transparency in reporting. For further information on Nature Research policies, see [Authors & Referees](#) and the [Editorial Policy Checklist](#).

Statistics

For all statistical analyses, confirm that the following items are present in the figure legend, table legend, main text, or Methods section.

n/a Confirmed

- The exact sample size (n) for each experimental group/condition, given as a discrete number and unit of measurement
- A statement on whether measurements were taken from distinct samples or whether the same sample was measured repeatedly
- The statistical test(s) used AND whether they are one- or two-sided
Only common tests should be described solely by name; describe more complex techniques in the Methods section.
- A description of all covariates tested
- A description of any assumptions or corrections, such as tests of normality and adjustment for multiple comparisons
- A full description of the statistical parameters including central tendency (e.g. means) or other basic estimates (e.g. regression coefficient) AND variation (e.g. standard deviation) or associated estimates of uncertainty (e.g. confidence intervals)
- For null hypothesis testing, the test statistic (e.g. F , t , r) with confidence intervals, effect sizes, degrees of freedom and P value noted
Give P values as exact values whenever suitable.
- For Bayesian analysis, information on the choice of priors and Markov chain Monte Carlo settings
- For hierarchical and complex designs, identification of the appropriate level for tests and full reporting of outcomes
- Estimates of effect sizes (e.g. Cohen's d , Pearson's r), indicating how they were calculated

Our web collection on [statistics for biologists](#) contains articles on many of the points above.

Software and code

Policy information about [availability of computer code](#)

Data collection

Sratoolkit/2.9.0 to download data from GEO database

Data analysis

We used the ImageJ 1.52a software to quantify the protein bands intensity, the 2D-ICAL v1.3.23 and ProteinPilot v3.0 software to analyze the results from MS, the MetaCore v6.33 software to analyze the results from RNAseq, FlowJo V10.6.1 software (Tree Star) to analyze the flow data, the Excel 2016 and GraphPad Prism 7 to do the graph figures and statistics. Bowtie v1.2; Bowtie 2 v2.2.9; MACS v1.4.2; MACS2 v2.1.1; STAR v2.5.4a; Cufflinks v2.2.1; GREAT v4.0.4; R v3.6.2; DIOPt v7.1; DOG v2.0.1; DAVID v6.8; REVIGO (web-based tool); ngsplot v2.61; HOMER v4.10.3; PAVIS (web-based tool), deepTools v2.5.3 were used to analyze the RNA-seq and ChIP-seq data. Metascape (web-based tool) was used to perform enrichment analysis. GEPPIA (web-based tool) and TIDE (web-based tool) were used to perform transcripts and survival analyses.

For manuscripts utilizing custom algorithms or software that are central to the research but not yet described in published literature, software must be made available to editors/reviewers. We strongly encourage code deposition in a community repository (e.g. GitHub). See the Nature Research [guidelines for submitting code & software](#) for further information.

Data

Policy information about [availability of data](#)

All manuscripts must include a [data availability statement](#). This statement should provide the following information, where applicable:

- Accession codes, unique identifiers, or web links for publicly available datasets
- A list of figures that have associated raw data
- A description of any restrictions on data availability

The next generation sequencing (NGS) data generated in this study have been submitted to the Gene Expression Omnibus Database (<https://www.ncbi.nlm.nih.gov/geo/>) with accession number GSE134510, GSE146557 and GSE146648. The data from mass-spectrometric analysis for identification of PD-L1 binding proteins and detection of acetylation were deposited in Japan Proteome Standard Repository/Database (JPOST) with the accession number: JPST000666/PXD015191 and

Field-specific reporting

Please select the one below that is the best fit for your research. If you are not sure, read the appropriate sections before making your selection.

Life sciences Behavioural & social sciences Ecological, evolutionary & environmental sciences

For a reference copy of the document with all sections, see nature.com/documents/nr-reporting-summary-flat.pdf

Life sciences study design

All studies must disclose on these points even when the disclosure is negative.

Sample size	RT-PCR assays in Fig. 6d, 7b, 7c, Extended Data Fig 5m, 6a, 6d and 6l-p were repeated for three times. Student t-test was used for significance analysis. For therapeutic syngeneic mouse model and other <i>in vivo</i> study, the numbers of mice are included in the figure legends of Fig. 3k, Fig. 7e-k and Extended Data Fig. 7a-c, 7e-g. No sample size calculations were performed. Sample size was determined according to our experience as well as literature reporting in terms of specific experiment.
Data exclusions	No data was excluded from the experiments.
Replication	All experimental findings were reliably reproduced. Multiple independent repeats were included for related experiments. Each experiment was performed for at least twice to make sure similar results are reproducible. Animal-related experiments have been done once.
Randomization	For the mouse assay in Fig. 3k, mice were randomized into two groups and injected with tumor cells. For the mouse assay in Fig. 7e-k, Extended Data Fig. 7a-c, 7e-g, mice after tumor cell injection were randomized into different groups and treated with indicated conditions.
Blinding	The investigators were not blinded to group allocation during data collection and/or analysis because we measured the value of tumor size and gave different treatments among groups.

Reporting for specific materials, systems and methods

We require information from authors about some types of materials, experimental systems and methods used in many studies. Here, indicate whether each material, system or method listed is relevant to your study. If you are not sure if a list item applies to your research, read the appropriate section before selecting a response.

Materials & experimental systems	Methods
n/a <input type="checkbox"/> Involved in the study <input type="checkbox"/> Antibodies <input type="checkbox"/> Eukaryotic cell lines <input checked="" type="checkbox"/> Palaeontology <input type="checkbox"/> Animals and other organisms <input checked="" type="checkbox"/> Human research participants <input checked="" type="checkbox"/> Clinical data	n/a <input type="checkbox"/> Involved in the study <input type="checkbox"/> ChIP-seq <input type="checkbox"/> Flow cytometry <input checked="" type="checkbox"/> MRI-based neuroimaging

Antibodies

Antibodies used	For immunoblot and immunoprecipitation, antibodies used in this study are below; anti-acetylated Lys (#9814, Cell Signaling Technology, CST), anti-human PD-L1, clone E1L3N (#13684, CST), anti-acetyl-K263-PD-L1 (acetyl-Lys263-PD-L1) antibody (generated by ABClonal Technology Biotech), anti-mouse PD-L1, clone EPR20529 (#ab213480, Abcam), anti-PD-L2 (#82723, CST), anti-VISTA (#64953, CST), anti-B7-H3 (#14058, CST), anti-B7-H4 (#14572, CST), anti-Galectin-9 (#54330, CST), anti-AIF (#5318, CST), anti-Histone H3 (#4499, CST), anti-MEK1/2 (#8727, CST), anti-GST (#2625, CST), anti-Tubulin (#T-5168, Sigma), Acetyl- α -Tubulin (Lys40) (#5335, CST), anti-c-Jun (#9165, CST), anti-Vimentin (#5741, CST), anti-E-Cadherin (#3195, CST), anti-KRT17 (#4534, CST), anti-KRT19 (#sc-376126, Santa Cruz Biotechnology), anti-HIP1R (#16814-1-AP, Proteintech Group), anti-HDAC2 (#57156, CST), rabbit polyclonal anti-Myc-tag (#2278, CST), mouse monoclonal anti-Myc-tag (#2276, CST), anti-HA (MMS-101P, BioLegend), anti-Flag (#F-3165, Sigma) or anti-GFP (#632381, Clontech). All these information was described in the immunoblot and immunoprecipitation section in methods. These primary antibodies except anti-acetyl-K263-PD-L1 antibody were used at 1:1,000 dilution in 5% non-fat milk for western blots. The anti-acetyl-K263-PD-L1 antibody was used at 1:200 dilution. PD-L1 antibodies generated in Dr. Freeman lab including: anti-human PD-L1 extracellular domain (clone 368A.5A4; 1:500 for WB), anti-human PD-L1 (clone 29E.12B1, 1 μ g/ml for IP), anti-mouse PD-L1 (clone 298B.3C6, 13 μ g/ml for IHC), anti-human PD-L1 (clone 9A11, 13 μ g/ml for IF); anti-mouse PD-L1 (clone 5C5, 10 μ g/ml for IF). Antibodies for flow cytometry: anti-mouse CD45 (30-F11, Brilliant Violet 605, Biolegend 103140, 2 μ g/ml), anti-mouse CD3 (145-2C11, Brilliant Violet 785, Biolegend 100355, 2 μ g/ml), anti-mouse (CD4, GK1.5, Brilliant Violet 650, Biolegend 100469, 1 μ g/ml)
-----------------	---

Validation

ml), anti-mouse CD8, (53-6.7, Brilliant Violet 711, Biolegend 100748, 2µg/ml), anti-mouse Granzyme B (GB11, Pacific Blue, Biolegend 515408, 5µl/100µl), anti-mouse FoxP3 (R16-715, PerCP-Cy5.5, BD563902, 2µg/ml), anti-mouse IFN-γ (XMG1.2, FITC, Biolegend 505806, 5µg/ml), anti-mouse TNF-α (MP6-XT22, APC, Biolegend 506308, 2µg/ml), anti-mouse IL-2 (JES6-5H4, Brilliant Violet 510, Biolegend 503833, 2µg/ml), anti-mouse IL-10 (JESS-16E3, PerCP-Cy5.5, Biolegend 505028, 2µg/ml)

We validated them according to manufacturers's Information . For the anti-acetyl-K263-PD-L1 (acetyl-Lys263-PD-L1) antibody, we used the non-acetylated peptides for the validation.

PD-L1 antibodies generated the Dr. Freeman lab are validated by previous studies with peer-reviewed publications, which have been cited in the Methods. anti-human PD-L1 (clone 368A.5A4, PubMed ID 26546452), anti-human PD-L1 (clone 29E.12B1, PubMed ID 29871885), anti-mouse PD-L1 (clone 298B.3C6, PubMed ID 26546452), anti-human PD-L1 (clone 9A11, PubMed ID 26546452); anti-mouse PD-L1 (clone 5C5, PubMed ID 14515254).

All other antibodies used in our study have been validated and detailed information could be found on the website from manufactures as listed below;

anti-acetylated Lys (#9441, Cell Signaling Technology, CST), https://en.cellsignal.jp/products/primary-antibodies/acetylated-lysine-antibody/9441?_=158993741434&Ntt=acetylated-ly&tahead=true
 anti-human PD-L1 (E1L3N) (#13684, CST), <https://en.cellsignal.jp/products/primary-antibodies/pd-l1-e1l3n-xp-rabbit-mab/13684>
 anti-mouse PD-L1 (EPR20529) (#ab213480, Abcam), <https://www.abcam.com/pd-l1-antibody-epr20529-ab213480.html>
 anti-PD-L2 (D7U8C) (#82723, CST), <https://en.cellsignal.jp/products/primary-antibodies/pd-l2-d7u8c-xp-rabbit-mab/82723>
 anti-VISTA (D1L2G) (#64953, CST), <https://en.cellsignal.jp/products/primary-antibodies/vista-d1l2g-xp-rabbit-mab/64953>
 anti-B7-H3 (D9M2L) (#14058, CST), <https://en.cellsignal.jp/products/primary-antibodies/b7-h3-d9m2l-xp-rabbit-mab/14058>
 anti-B7-H4 (D1M8I) (#14572, CST), <https://en.cellsignal.jp/products/primary-antibodies/b7-h4-d1m8i-xp-rabbit-mab/14572>
 anti-Galectin-9 (D9R4A) (#54330, CST), <https://en.cellsignal.jp/products/primary-antibodies/galectin-9-d9r4a-xp-rabbit-mab/54330>
 anti-AIF (D39D2) (#5318, CST), <https://en.cellsignal.jp/products/primary-antibodies/aif-d39d2-xp-rabbit-mab/5318>
 anti-Histone H3 (D1H2) (#4499, CST), <https://en.cellsignal.jp/products/primary-antibodies/histone-h3-d1h2-xp-rabbit-mab/4499>
 anti-MEK1/2 (D1A5) (#8727, CST), <https://en.cellsignal.jp/products/primary-antibodies/mek1-2-d1a5-rabbit-mab/8727>
 anti-GST (91G1) (#2625, CST), <https://www.cellsignal.jp/products/primary-antibodies/gst-91g1-rabbit-mab/2625>
 anti-Tubulin (#T-5168, Sigma), <https://www.sigmal Aldrich.com/catalog/product/sigma/t5168?lang=en®ion=US>
 Acetyl- α -Tubulin (Lys40) (D20G) (#5335, CST), <https://en.cellsignal.jp/products/primary-antibodies/acetyl-a-tubulin-lys40-d20g3-xp-rabbit-mab/5335>
 anti-c-Jun (60A8) (#9165, CST), <https://en.cellsignal.jp/products/primary-antibodies/c-jun-60a8-rabbit-mab/9165>
 anti-Vimentin (D21H3) (#5741, CST), <https://en.cellsignal.jp/products/primary-antibodies/vimentin-d21h3-xp-rabbit-mab/5741>
 anti-E-Cadherin (24E10) (#3195, CST), <https://en.cellsignal.jp/products/primary-antibodies/e-cadherin-24e10-rabbit-mab/3195>
 anti-KRT17 (D73C7) (#4543, CST), <https://en.cellsignal.jp/products/primary-antibodies/keratin-17-d73c7-rabbit-mab/4543?site-search-type=Products>
 anti-KRT19 (A-3) (#sc-376126, Santa Cruz Biotechnology), https://www.scbt.com/p/cytokeratin-19-antibody-a-3?productCanUrl=cytokeratin-19-antibody-a-3&_requestid=170294
 anti-HIP1R (#16814-1-AP, Proteintech Group), <https://www.ptglab.com/Products/HIP1R-Antibody-16814-1-AP.htm>
 anti-HDAC2 (D6S5P) (#57156, CST), <https://en.cellsignal.jp/products/primary-antibodies/hdac2-d6s5p-rabbit-mab/57156>
 rabbit polyclonal anti-Myc-tag (71D10) (#2278, CST), <https://en.cellsignal.jp/products/primary-antibodies/myc-tag-71d10-rabbit-mab/2278>
 mouse monoclonal anti-Myc-tag (9B11) (#2276, CST), <https://en.cellsignal.jp/products/primary-antibodies/myc-tag-9b11-mouse-mab/2276>
 anti-HA (16B12) (MMS-101P, BioLegend), <https://www.biologend.com/en-us/products/purified-anti-ha-11-epitope-tag-antibody-11374>
 anti-Flag (#F-3165, Sigma), <https://www.sigmal Aldrich.com/catalog/search?term=F3165&interface=All&N=0&mode=match%20partialmax&lang=en®ion=US&focus=product>
 or anti-GFP (JL-8) (#632381, Clontech), <https://www.takarabio.com/products/antibodies-and-elisa/fluorescent-protein-antibodies/green-fluorescent-protein-antibodies>
 anti-mouse CD45 (30-F11) <https://www.biologend.com/en-us/products/brilliant-violet-605-anti-mouse-cd45-antibody-8721>
 anti-mouse CD3 (145-2C11) <https://www.biologend.com/en-us/products/brilliant-violet-785-anti-mouse-cd3epsilon-antibody-12081>
 anti-mouse (CD4, GK1.5) <https://www.biologend.com/en-us/products/brilliant-violet-650-anti-mouse-cd4-antibody-16780>
 anti-mouse CD8, (53-6.7) <https://www.biologend.com/en-us/products/brilliant-violet-711-anti-mouse-cd8a-antibody-7926>
 anti-mouse Granzyme B (GB11)<https://www.biologend.com/en-us/products/pacific-blue-anti-human-mouse-granzyme-b-antibody-8612>
 anti-mouse FoxP3 (R16-715) <https://www.bdbiosciences.com/eu/applications/research/t-cell-immunology/regulatory-t-cells/intracellular-markers/cell-signalling-and-transcription-factors/mouse/percp-cy55-rat-anti-mouse-foxp3-r16-715/p/563902>
 anti-mouse IFN-γ (XMG1.2) <https://www.biologend.com/en-us/products/fitc-anti-mouse-ifn-gamma-antibody-995>
 anti-mouse TNF-α (MP6-XT22) <https://www.biologend.com/en-us/products/apc-anti-mouse-tnf-alpha-antibody-975>
 anti-mouse IL-2 (JES6-5H4) <https://www.biologend.com/en-us/products/brilliant-violet-510-anti-mouse-il-2-antibody-9274>
 anti-mouse IL-10 (JESS-16E3) <https://www.biologend.com/en-us/products/percp-cyanine5-5-anti-mouse-il-10-antibody-8143>

Eukaryotic cell lines

Policy information about [cell lines](#)

Cell line source(s)

The cell lines we used in this study are below: HEK293T, Hs578T, MDA-MB-231, MDA-MB-436, A375, SW839, RAW264, MEFs, B16F10, MC38, BT-549, HCC1937, HCC1954, SKBR3, BT-20, MCF7, MDA-MB-468, T47D and ZR75-1, DU145 and CT26

cells. MDA-MB-231 PD-L1 KO cells and BT549 PD-L1 KO cells were kindly gifted from Dr. Mien-Chie Hung. The sources and information of cell line are shown in the Supplementary Table 8.

Authentication

The authentication status of all cell lines is summarized in the Supplementary Table 8. Hs578T, MDA-MB-231, MDA-MB-436, SW839, MC38, BT-549, HCC1937, HCC1954, SKBR3, BT-20, MCF7, MDA-MB-468, T47D and ZR75-1 are authenticated. Other line including HEK293T, CT26, B16F10, RAW264.7 are newly purchased from ATCC.

Mycoplasma contamination

Yes. Cell lines used in this study were routinely tested to be negative for mycoplasma

Commonly misidentified lines (See [ICLAC](#) register)

Among all the cell lines, only BT-20 is listed by ICLAC in the Table 2, indicates that "cell lines where some stocks have been shown to be misidentified, but where authentic stock is known to exist". We have shown the ATCC authentication report (STR method, 100% match to ATCC cell line HTB-19 (BT-20)) in the Extended Data Fig.1b. We involved the BT-20 cell line in our study because we wanted to validate our findings in as many as breast cancer cell lines we can obtain.

Animals and other organisms

Policy information about [studies involving animals](#); [ARRIVE guidelines](#) recommended for reporting animal research

Laboratory animals

The 6-8 week-old female C57BL/6 mice, BALB/c female mice (Jackson Lab, MI) and 6-8 week-old female nude mice (T-cell deficient, Taconic # NCRNU-F) were used for the implanted tumor assays. For MC38 model, mice were grouped into four groups: control antibody, PD-1 mAb (clone 29F.1A12), HDAC2 inhibitor (Satacruzamate A, Sellechem S7595) and PD-1 mAb plus HDAC2 inhibitor. For CT26 model, mice were grouped into two groups (control antibody and PD-1 mAb). The control and PD-1 mAb treatments were conducted by intraperitoneal injection (200 µg/mouse in 200 µl HBSS saline buffer) every three days for a total of 8 injections. The HDAC2 inhibitor treatment was given by intraperitoneal injection once a day with a dosage of 25 mg/kg (in 5% DMSO, 5% PEG 300, 5% Tween 80 in ddH₂O) for three weeks with a break every week for one day.

Wild animals

The study does not involve wild animals.

Field-collected samples

NO.

Ethics oversight

The study is compliant with all relevant ethical regulations regarding animal research. Animal studies were approved by Dana-Farber Cancer Institute Institutional Animal Care and Use Committee (IACUC; protocol number 04-047) or Beth Israel Deaconess Medical Center (BIDMC) Institutional Animal Care and Use Committee (IACUC: Protocol #043-2015) and performed in accordance with guidelines established by NIH Guide for the care and use of laboratory animals.

Note that full information on the approval of the study protocol must also be provided in the manuscript.

ChIP-seq

Data deposition

Confirm that both raw and final processed data have been deposited in a public database such as [GEO](#).

Confirm that you have deposited or provided access to graph files (e.g. BED files) for the called peaks.

Data access links

May remain private before publication.

To review GEO accession GSE146648, go to <https://www.ncbi.nlm.nih.gov/geo/query/acc.cgi?acc=GSE146648>, and enter token 'mfzmzsmmlfqptez' into the box.

Files in database submission

PDL1_ChIPseq_Rep1_R1.fastq.gz
PDL1_ChIPseq_Rep1_R2.fastq.gz
Input_Rep1_R1.fastq.gz
Input_Rep1_R2.fastq.gz
PDL1_ChIPseq_Rep2.fastq.gz
Input_Rep2.fastq.gz
Rep1_peaks.broadPeak
Rep2_peaks.broadPeak

Genome browser session (e.g. [UCSC](#))

[https://genome.ucsc.edu/cgi-bin/hgTracks?](https://genome.ucsc.edu/cgi-bin/hgTracks?db=hg38&lastVirtModeType=default&lastVirtModeExtraState=&virtModeType=default&virtMode=0&nonVirtPosition=&position=chr1%3A1719970%2D2547969&hgsid=813455665_1FNlJmzihMHhhVL62QWkNH0vhV4W)
db=hg38&lastVirtModeType=default&lastVirtModeExtraState=&virtModeType=default&virtMode=0&nonVirtPosition=&position=chr1%3A1719970%2D2547969&hgsid=813455665_1FNlJmzihMHhhVL62QWkNH0vhV4W

Methodology

Replicates

Two biological replicates.

Sequencing depth

Total number of reads	Uniquely mapped reads	Length of reads (nt)	Single or paired-end
PD-L1_ChIPseq_Rep1	58973013	35192761	41 Paired-end
Input_Rep1	69864972	46566465	41 Paired-end
PD-L1_ChIPseq_Rep2	119150413	68955199	75 Single
Input_Rep2	115923858	68290224	75 Single

Antibodies

anti-HA-tag antibody (Abcam, ab9110)

Peak calling parameters

```
For Rep1:  
macs2 callpeak -t PDL1_ChIPseq_Rep1.bam -c Input_Rep1.bam -f BAMPE -g hs -n PDL1_Rep1 --broad --broad-cutoff 0.05 --outdir .  
For Rep2:  
macs2 callpeak -t PDL1_ChIPseq_Rep2.bam -c Input_Rep2.bam -f BAM -g hs -n PDL1_Rep2 --broad --broad-cutoff 0.05 --outdir .
```

Data quality

FDR 5% peaks:
Rep1: 166628
Rep2: 93618

Software

Bowtie 2 v2.2.9 were used for the genome alignment of ChIP-seq raw reads;
MACS2 v2.1.1 were used for calling ChIP-seq peaks;
GREAT v4.0.4 was used to assign ChIP-seq peaks to genes;
PAVIS software was used for the peak gene annotation;
R v3.6.2 was used for statistical analyses and plotting figures (Fig 6i&j and Ext fig 5m)
ngsplot v2.61 was used for generating metagene plot (Fig 6g) and heatmaps (Fig 6h)

Flow Cytometry

Plots

Confirm that:

- The axis labels state the marker and fluorochrome used (e.g. CD4-FITC).
- The axis scales are clearly visible. Include numbers along axes only for bottom left plot of group (a 'group' is an analysis of identical markers).
- All plots are contour plots with outliers or pseudocolor plots.
- A numerical value for number of cells or percentage (with statistics) is provided.

Methodology

Sample preparation

Nine days after the treatment of MC38 tumours with indicated condition, tumor infiltrating lymphocytes (TILs) were isolated and stained. For stimulation, Cells were incubated with cell stimulation cocktail (PMA and Ionomycin) plus protein transport inhibitor (Brefeldin A and Menesin) for 4 hours.

Instrument

BD LSR Fortessa X-20

Software

Used BD FACSDIVA software for collecting data. All analysis was performed using FlowJo_V10.6.1 software (Tree Star).

Cell population abundance

N/A

Gating strategy

Gate cells exclude dead cells and debris based on cells size, then gate live cells based on Live-Dead NIR negative cells, then gate CD45+ cells, then gate CD45+CD3+ cells, then gate CD45+CD3+CD8+ cells and CD45+CD3+CD4+ cells. Cytokine expression were determined in the populations of CD45+CD3+cells.

Tick this box to confirm that a figure exemplifying the gating strategy is provided in the Supplementary Information.